VYSOKÉ UČENÍ TECHNICKÉ V BRNĚ

BRNO UNIVERSITY OF TECHNOLOGY

FAKULTA STROJNÍHO INŽENÝRSTVÍ
ÚSTAV MATERIÁLOVÝCH VĚD A INŽENÝRSTVÍ

FACULTY OF MECHANICAL ENGINEERING
INSTITUTE OF MATERIALS SCIENCE AND ENGINEERING

STUDY OF TRANSITION FROM OPEN TO CLOSED POROSITY STAGE DURING SINTERING OF ADVANCED CERAMIC MATERIALS

STUDIUM PŘECHODU ZE STADIA OTEVŘENÉ DO STADIA UZAVŘENÉ PÓROVITOSTI PŘI SLINOVÁNÍ POKROČILÝCH KERAMICKÝCH MATERIÁLŮ

DIPLOMOVÁ PRÁCE
MASTER'S THESIS

AUTOR PRÁCE   Bc. TOMÁŠ SPUSTA
AUTHOR

VEDOUCÍ PRÁCE   prof. RNDr. KAREL MACA, Dr.
SUPERVISOR

BRNO 2015

Vysoké učení technické v Brně, Fakulta strojního inženýrství

Ústav materiálových věd a inženýrství
Akademický rok: 2014/2015

ZADÁNÍ DIPLOMOVÉ PRÁCE

student(ka): Bc. Tomáš Spusta

který/která studuje v **magisterském navazujícím studijním programu**

obor: **Materiálové inženýrství (3911T011)**

Ředitel ústavu Vám v souladu se zákonem č.111/1998 o vysokých školách a se Studijním a zkušebním řádem VUT v Brně určuje následující téma diplomové práce:

Studium přechodu ze stadia otevřené do stadia uzavřené pórovitosti při slinování pokročilých keramických materiálů

v anglickém jazyce:

Study of transition from open to closed porosity stage during sintering of advanced ceramic materials

Stručná charakteristika problematiky úkolu:

Student bude teoreticky a experimentálně studovat evoluci pórů v průběhu slinování oxidových keramických materiálů v oblasti přechodu z fáze otevřené do fáze uzavřené pórovitosti. Toto studium umožní stanovit hranici relativní hustoty, která je nutná pro efektivní použití HIPování umožňující výrobu keramických výrobků s vysokou relativní hustotou při minimalizaci růstu zrn – například transparentních keramických materiálů.

Cíle diplomové práce:

Student na základě literární rešerše teoreticky popíše termodynamické podmínky, při nichž dochází k přechodu ze stadia otevřené do stadia uzavřené pórovitosti. V další části své práce provede řadu slinovacích experimentů s cílem tyto teoretické poznatky ověřit a rozšířit pro různé oxidové keramické materiály (Al2O3, ZrO2, CeO2, MgAl2O4). Práce má praktické využití pro nalezení vhodných podmínek pro následné HIPování těchto materiálů a přípravu hutných keramik se zlepšenou mikrostrukturou, např.strukturních nebo transparentních keramických materiálů.

Seznam odborné literatury:

1. M.N. Rahaman: Sintering of Ceramics, CRC Press, 2008
2. http://www.sciencedirect.com/science/journal/13871811/151
3. http://apps.isiknowledge.com

Vedoucí diplomové práce: prof. RNDr. Karel Maca, Dr.

Termín odevzdání diplomové práce je stanoven časovým plánem akademického roku 2014/2015.

V Brně, dne 11.3.2015

L.S.

_____   _____
prof. Ing. Ivo Dlouhý, CSc.   doc. Ing. Jaroslav Katolický, Ph.D.
Ředitel ústavu   Děkan fakulty

ABSTRACT

Hot isostatic pressing (HIP) is advanced technique for processing of fully dense ceramic materials, which have variety of structural (e.g. cutting tools), biological (e.g. dense bone and joint implants) or functional (e.g. transparent windows and armours) applications. For successful post-HIP treatment the presintered samples have to be air tight, i.e. without open porosity. The research in the field of transition from open to closed porosity stage is therefore very important, but it is only rarely published in the relevant literature. The experimental and theoretical study of this phenomena was therefore the main goal of this work.

The analyses of theoretical models show that pore transformation from open to closed porosity is material characteristic which varies only with dihedral angle, independently on particle size or shaping process, and occurs from 92.6% t.d. to 93.7% t.d. for used materials (alumina, zirconia and magnesia-alumina spinel). These theoretical calculations were compared with experimental data obtained from the literature and with experimental data of this thesis with successful match for cubic systems (spine and cubic zirconia). The experimental results obtained for alumina were in good agreement with experimental data published in the literature (95-96% t.d.), but they were higher than the values calculated from theoretical models. Several hypotheses for explanation of this issue were described and some approaches of resolving this topic were proposed.

KEY WORDS

Oxide ceramics, sintering, post-HIPing, open porosity, closed porosity

ABSTRAKT

Lisovanie za tepla (HIP) je pokročilá technológia pre výrobu plne hutných keramických materiálov, ktoré majú množstvo štruktúrnych (napr. rezné nástroje), biologických (napr. implantáty hutných kostí a kĺbov) alebo funkčných (napr. transparentné štíty a okná) aplikácií. Pre úspešné použitie tejto technológie je potrebné, aby predspekané vzorky boli plynotesné, teda bez otvorených pórov. Výskum zaoberajúci sa premenou otvorených pórov na uzatvorené je preto veľmi dôležitý, avšak iba málo publikovaný v odbornej literatúre. Preto bolo experimentálne a teoretické štúdium tohto javu hlavným cieľom diplomovej práce.

Analýzy teoretických modelov ukazujú, že transformácia z otvorenej na uzatvorenú pórovitosť je materiálová charakteristika, ktoré sa mení iba s dihedrálnym uhlom, nezávisle na veľkosti častíc prášku alebo na spôsobe tvarovania a nastáva od 92.6% t.d. do 93.7% t.d pre daný materiál (oxid hlinitý, oxid zirkoničitý a horečnato-hlinitý spinel). Tieto teoretické výpočty boli porovnané s experimentálnymi dátami z literatúry a dátami z experimentálnej časti diplomovej práce s úspešnou zhodou pre kubické systémy (spinel a kubický oxid zirkoničitý). Výsledky experimentov s oxidom hlinitým boli v dobrej zhode s experimentálnymi dátami publikovanými v literatúre, ale boli vyššie ako teoretické hodnoty. Na objasnenie týchto odlišností bolo vytvorených niekoľko hypotéz a tiež boli navrhnuté spôsoby riešenia tejto témy.

KĽÚČOVÉ SLOVÁ

Oxidová keramika, spekanie, post-HIPing, otvorená pórovitosť, uzatvorená pórovitosť

BIBLIOGRAPHIC CITATION

SPUSTA, T. *Studium přechodu ze stadia otevřené do stadia uzavřené pórovitosti při slinování pokročilých keramických materiálů.* Brno: Vysoké učení technické v Brně, Fakulta strojního inženýrství, 2015. 60 s. Vedoucí diplomové práce prof. RNDr. Karel Maca, Dr..

DECLARATION

I declare that this master's thesis was worked out on my own using mentioned literature and under supervision of above named supervisor.

In Brno on the 29th of May 2015

....
Bc. Tomáš Spusta

ACKNOWLEDGEMENTS

TABLE OF CONTENT

1 INTRODUCTION

In general knowledge ceramics are perceived as objects of daily life such as mugs, plates and other kinds of pottery, sanitary ceramics, tile contractors, building material or ceramic knifes and kitchen equipment. However, there is huge branch of ceramic materials more or less invisible for ordinary people. This branch called advanced ceramics is characterized by high purity of chemical composition, engineered microstructure, chemical inertness, extreme hardness, high melting temperature and other properties suitable for specialized tasks in difficult conditions.

Properties of advanced ceramics (given by chemical structure and strong ionic and covalent bonds) predestine them for variety purposes, namely for structural ceramics [1] (e.g. cutting inserts, ball bearings, automobile valves, turbines, plates for ballistic vests), bioceramics [2, 3] (e.g. dental and bone implants, joint replacements), electroceramics [4] (e.g. ferroelectrics, ferrites, solid electrolytes, magnetoelectrics), optical ceramics [1] (e.g. lasers, sensor protections, transparent armours) and much more.

Demands of modern world indicate that material with only one superb property is not capable to compete in challenging projects. Even two excellent attributes combined are often not enough. This puts material engineers, chemists and other scientists in front of a difficult task: "How to fuse material properties which are mostly opposite by nature?". For example: High abrasive resistance and solid ductility combined with transparency for white (visible) light. This example is not mentioned by accident, material with these capabilities is really suitable for transparent ceramic armour. Transparent ceramics are made from super pure chemical precursors and they are fabricated by quite sophisticated technology. There are only a few possibilities of how to produce not only translucent, but highly transparent bulk ceramics. They combine external pressure and elevated temperature.

One of the technologies to produce transparent ceramics with required microstructure (density and grain size), thus transparency and mechanical properties, is a process called "post-HIPing". In general, this process can be divided into several stages. If powder synthesis and shaping steps are not account (although they have the same importance as any of the remaining steps), it is pressureless presintering to close up open porosity in the ceramics before final step, called HIP, is used to remove remaining closed porosity. HIP stands for "Hot Isostatic Press" (combination of high temperature and high gas pressure), which is kind of pressure assisted sintering.

Key step in post-HIPing process is to find conditions when pores are closed (or better to say "isolated"). Pore closure phenomena are characterized by transformation of sintered material, which experiences transition from the second to the third stage of sintering. This shift occurs at high relative densities according to sintering theory and literature data [6-8] this threshold value is shown as generalised number (usually 92% t.d.) and independent of sintered material. However, in practice the critical density (the relative density of sample when open pores transform and in sample only closed pores exist) is not uniform, neither it is the same for all materials as can be seen in various articles about post-HIPing treatment [9-22] (articles are mainly focused on transparent ceramics).

Goal of this master's thesis is to significantly enrich existing experimental database in this field using different ceramic materials (alumina, tetragona and cubic zirconia, alumina-magnesia spinel) with different particle size and microstructure of ceramic green body and in addition to compare obtained experimental results with theoretical models published in the literature.

2 THEORETICAL BACKGROUND

2.1 Powder Preparation

2.1.1 Characteristics of Loose Powder

Majority of advanced ceramic products are made from ceramic powder, mostly commercially produced with standardized properties, such as particle size, particle size distribution, particle shape, particle structure and chemical composition. Even with this knowledge, ceramic powders are not completely suitable for manufacturing ceramic components. To meet the desired characteristics, the powder is treated by shaping and consolidation techniques [3].

Primary particles in submicrometer-sized and nanometer-sized powder often do not exist in single-crystal entities dispersed homogeneously, but they create agglomerates (*Figure 1A*) and aggregates (*Figure 1B*). The difference between agglomerates and aggregates is not strictly defined, but generally speaking primary particles in an aggregate are bound together more strongly and more densely with less inter-agglomerate porosity than in an agglomerate. Non-uniform particle packing might cause various defects, pore distribution, cracks, even exaggerated grain growth and warpage of sintered ceramic parts [23].
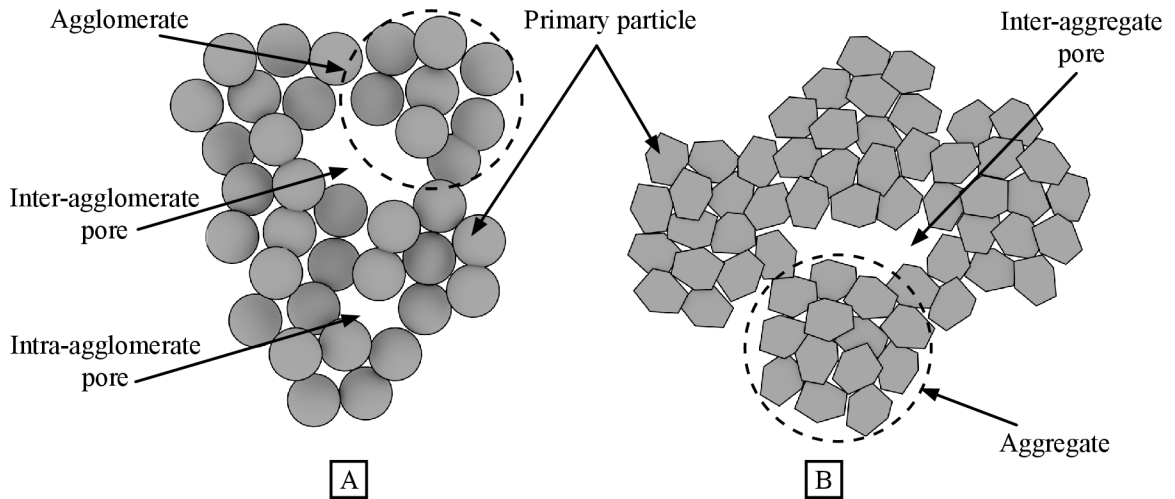
Figure 1: Schematic illustration of powder types: A) Agglomerated; B) Aggregated.

There are several factors influencing the formation of agglomerates and aggregates. However, most of them can be eliminated by an appropriate synthesis adjustments, except for van der Waals forces. Van der Waals (VdW) forces are always attractive forces between powder particles. VdW forces are linearly dependent on particle size accordingly to Eq. 1:

$$F_{VdW} = \frac{AR}{12D^2},\qquad(1)$$

where A is Hamaker constant (describing dielectric properties of the materials), R is the particle radius and D is the distance between particle surfaces. The smaller dimension of particles, the stronger effect the VdW forces will have, e.g., for particles (spherical) with a diameter under 1 μm, the VdW forces are so big that they exceed gravitation force by 5-7 orders of magnitude. In work experience this means that particles will rather stick together and form

structures mentioned above, than exist separately. According to these observations to prevent fine powder particles from agglomerating, the close contact between particles must be avoided. This can be accomplished by a dispersant adsorbed on the surface of particles. The dispersant rises the repulsive forces when particles approach each other and prevents close contact and therefore agglomeration [3].

Elimination of agglomerated particles and production of fine powder is the most important task in this processing step. The most effective procedures for deagglomeration of particles and for particle dispersion have proved to be ball milling and attrition milling [3]. Furthermore, these milling techniques provide possibilities to accomplish additional improvement of powder, such as particle size adjustment, coating the particle surface with surface-active additives, mixing of multiple powders, mixing the powder with a binder and/or with other processing additives, particle dispersion and stabilization in a solvent [3].

Intensive mechanical movement and impacts of grinding media (usually ceramic balls, rods or small cylinders) cause destruction of agglomerates. *Figure 2* and *Figure 3* show the ball milling and the attrition milling schematics. The milling can be dry (without liquid solvent) or wet (with liquid solvent) according to the subsequent processing steps [3].
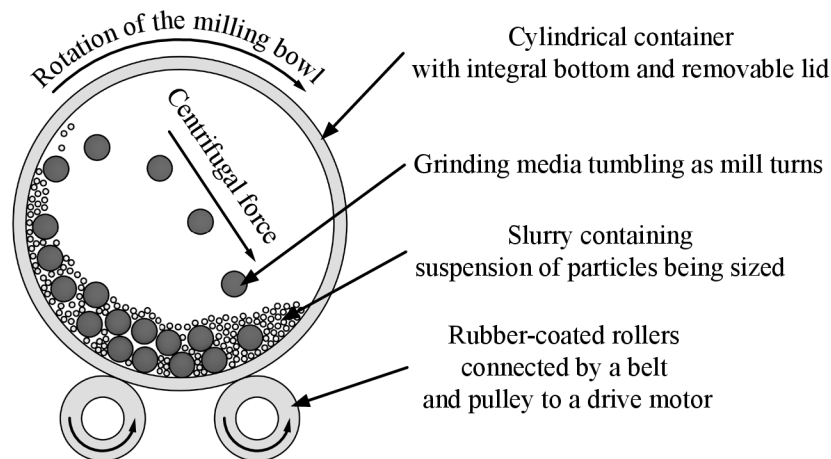
Figure 2: Ball milling illustration.
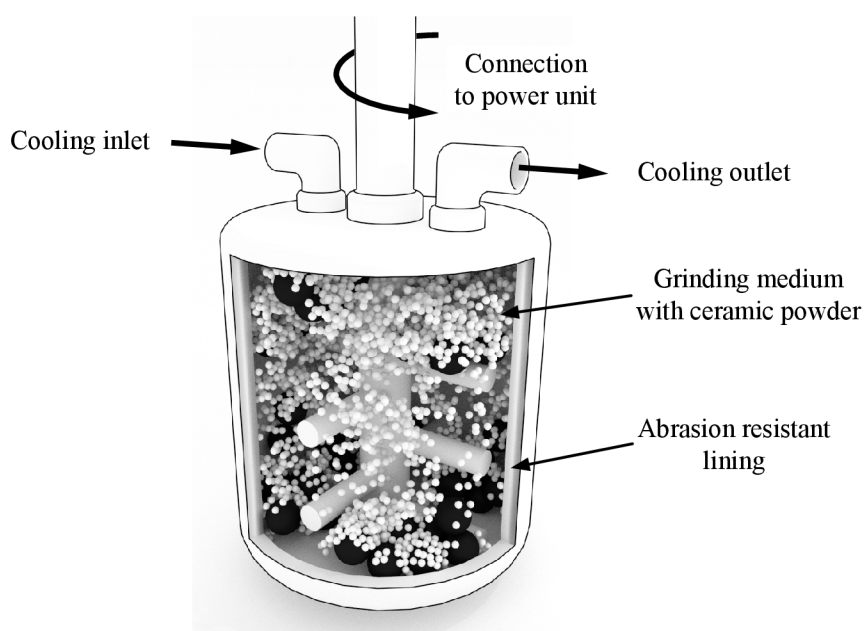
Figure 3: Attrition milling illustration.

2.1.2 Powder granulation

Due to attractive forces (as discussed above), fine powders form agglomerates and do not flow easily. This property of powder causes difficulties when filling the die or mould and compacting them homogeneously. Therefore, fine powders are usually granulated, commonly by spray-drying a well-dispersed ceramic slurry. The slurry is sprayed into a drying chamber with a stream or hot air. Small slurry droplets dry and produce spherical powder granules of 20-250 μm in size (e.g. spray-dried zirconia powder in *Figure 4*) [3].

The granules flow easily and regularly fill the die or mould. During compaction (*Figure 5*) granules deform and eliminate the inter-granular porosity and keep the intra-granular homogeneity. To ensure plasticity of the granules and sufficient handling strength of pressed compact about 3-5 wt.% of the organic additives are typically used [3].
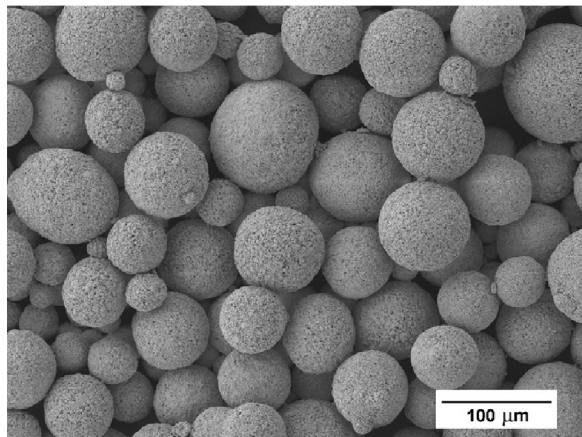
Figure 4: Spray-dried zirconia powder [3].

In this master's thesis only dry shaping methods (namely cold isostatic pressing) were used, therefore no additional organic additives except those in powder itself participate on shaping process. However, even minimal volume of binder has to be removed before sintering, which is done in furnace heated on approximately 800 °C. Removing the binder before sintering in different furnace prevents contamination of furnaces.
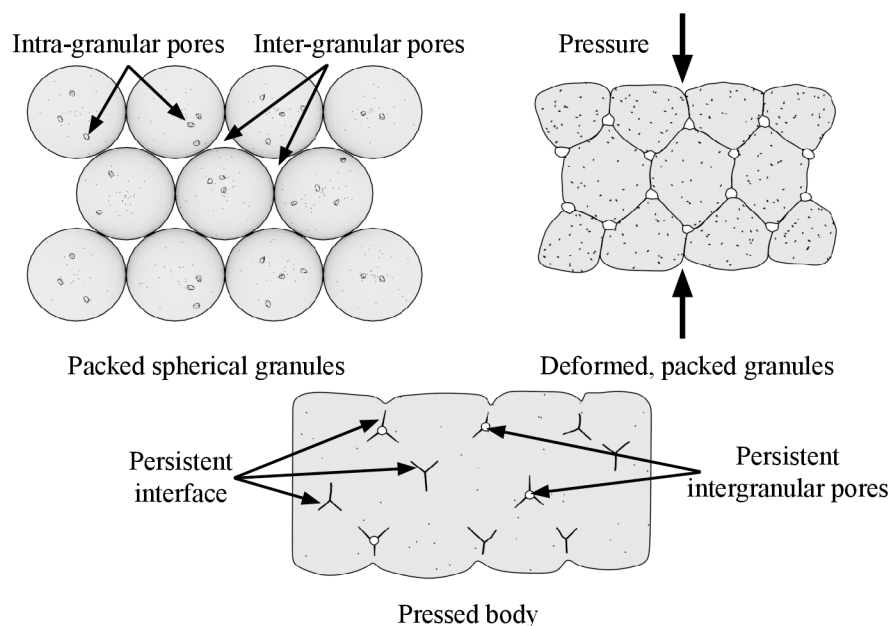
Figure 5: Illustration of powder deformation during pressing.

2.2 Powder Shaping and Forming

The purpose of the most of shaping and forming methods is to fabricate a body with compact shape, consisting of consolidated powder. This is called "green body". The shaping-forming techniques are required to provide a green body with following properties: homogeneous structure of ceramic green body, minimal defect size in the green body (bubbles, cracks, warpage, impurities, etc.), minimal requirements on the machining of the final sintered body [3].

There are numerous possibilities and techniques for shaping the powder, divided into numerous classes [3]: wet shaping, dry shaping, plastic shaping, etc. However, in this diploma thesis only dry methods were used, namely cold isostatic pressing, therefore they will be explained more deeply.

2.2.1 Uniaxial Pressing

During uniaxial pressing ceramic powder is compacted/pressed in a rigid die by applying pressure from one direction by a piston or a punch. Uniaxial pressing is mainly suitable for low-height and cylindrical bodies. Pressing large bodies usually results in inhomogeneities in packing of ceramic particles due to die-particle friction [24]. During sintering, inhomogeneities (lower density areas) will either shrink more than the surrounding areas or will not be densified completely. Both can lead to deformations or cracks in the sintered product [3].

2.2.2 Cold Isostatic Pressing

Isostatic pressing overcomes some limitations of uniaxial pressing (mainly by applying pressure from all directions), which makes this method more usable for complex shapes of green body. In isostatic pressing, uniform hydrostatic pressure is applied to the powder closed in a flexible rubber or plastic mould. Unfortunately, because of flexible mould, this method is not capable to create green body with outher dimensions [3].

There are two types of cold isostatic pressing widely used: wet-bag and dry-bag. Wet-bag is characterized by shaped flexible mould, where powder is sealed, immersed in liquid in a high-pressure vessel. The liquid in vessel is pressurized and pressure is transmitted through the mould to the powder, which results in compaction. After compaction, pressure is released and the compacted body is removed from mould. The main advantage of this method is higher packing uniformity than in uniaxial pressing. The most common pressure used in production is 200-300 MPa, although pressure up to 1000 GPa can be used [3].

Dry-bag is characterized by a rubber mould tightly connected with pressure vessel. This results in the pressurized liquid not acting isostaticaly, so the mould must be carefully designed to ensure homogeneous particle packing in the powder compact. Advantage of dry-bag alternative is possibility of automation of the pressing process and therefore increase speed of production of green bodies [3].

2.3 Sintering

Sintering is a physical process to produce density controlled materials and components from ceramic or/and metal powders by applying thermal energy [7]. It is consequent process after forming and shaping powder. The main role of sintering is to increase density of the product by decreasing of surface energy to the highest possible level, ideally to 100% of theoretical density. However, there are exceptions such as bio-scaffolds, bone replacements, filters, etc., which require porous structure (less than 100% t.d.) and provide excellent evidence how variable sintering process can be. In general, sintering could be divided into two types: liquid phase sintering and solid state sintering.

2.3.1 Liquid Phase Sintering

Liquid phase sintering is characteristic by the temperature of sintering above melting temperature of one (or more) of the reactants, or creation of the glass phase along the grain boundaries. In the presence the liquid phase the microstructure change is fast because of fast material transport through the liquid and capillary forces enhancing the densifying process [7].

2.3.2 Solid State Sintering

Solid state sintering is the main process studied in this master's thesis, so following review will be focused primarily on this type of sintering, its theory and practice. Solid state sintering is specific by sintering temperature under the melting point of the powder. In theory, powder is often idealised to spheres with the same diameter and with such geometry in mind, the whole process of sintering (coarsening and densification) is treated [7].

Sintering is usually described by 3 stages (*Figure 6*) with corresponding theory approaches and models. Characteristic phenomena for the first stage is enlargement of contact points of neighbour powder particles and creation of so-called necks. In the second stage, necks grow and create tubular interconnected pore network. In the third stage the tubular pores from the second stage collapse and form spherical or lenticular pores primarily on grain edges [26].
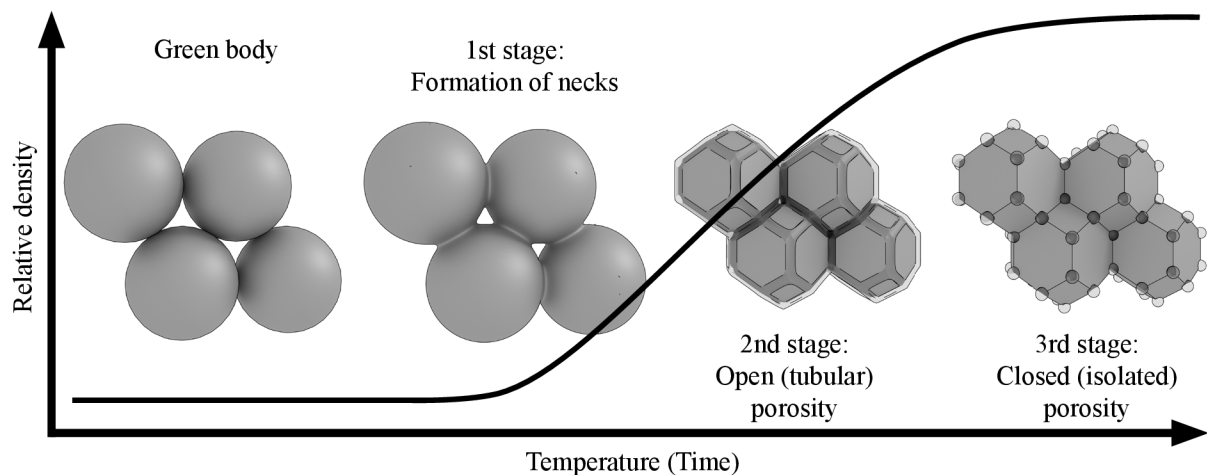
Figure 6: Stages of sintering.

The First Stage of Sintering

The initial sintering stage consists of fairly rapid interparticle neck growth by diffusion, vapour transport, plastic flow or viscous flow. Large initial differences in surface curvature are removed in this stage and shrinkage (or densification) accompanies neck growth densifying mechanisms. For a powder system consisting of spherical particles, the initial stage is

characteristic by neck growth in contact areas between particles. It is assumed to last until the radius of the neck between the particles has reached the value of ~0.4-0.5 of particle radius. For a powder system with an initial density of 50-60% t.d. this corresponds to a linear shrinkage of 3 to 5% or an increase in density to ~65% t.d. when densifying mechanisms dominate [6].

The Second Stage of Sintering

The intermediate stage begins when the tubular pores have reached their equilibrium shapes as dictated by the surface and interfacial tensions. The pore phase is still interconnected and open to the outer surface. In the sintering models, the structure is usually idealized in terms of cylinder-like array of porosity sitting along the edges. Densification is assumed to occur by the pores simply shrinking to reduce their cross section. Finally, pores become unstable and pinch off, leaving isolated pores. This constitutes the beginning of the final stage. The intermediate stage normally covers the major part of the sintering process, and it is taken to end when the density is ~90% of theoretical density [6].

The Third Stage of Sintering

The microstructure in the final stage could evolve in different ways, but one of the simplest descriptions is, that the third stage begins when the pores pinch off and become isolated at the grain corners. In this simple description the pores are assumed to shrink continuously and may disappear altogether, which leaves material with 100% of theoretical density [6].
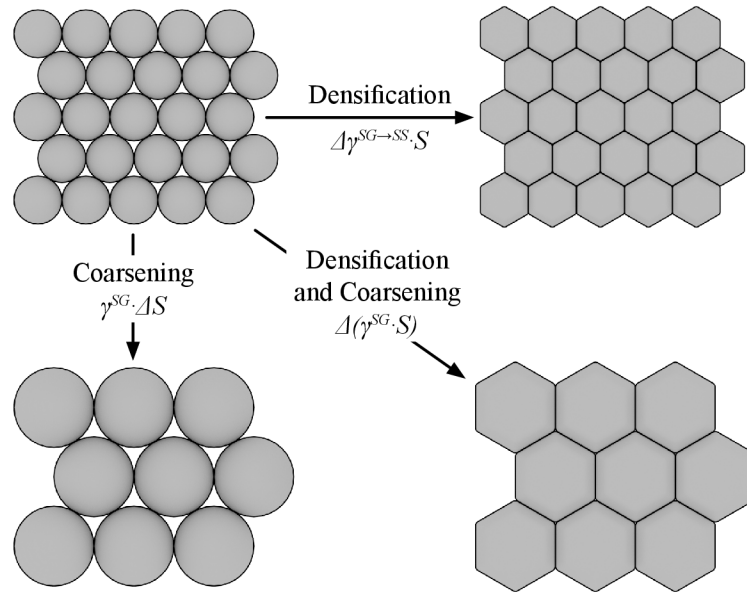
Figure 7: Scheme of the decrease of the surface energy ($\gamma^{SG}S$) during sintering and coarsening.

2.3.3 The driving force of sintering

The thermodynamic driving force for sintering is the reduction of the surface energy. The loose particles have bigger free surface, thus the dominant form of interfacial energy is γ^{SG}, energy of gas and solid interface, which is bigger than interfacial energy of grain boundaries γ^{SS}. Therefore, it is required, in terms of lowering the energy of system, to change loose particles to grains. Total surface energy change can be expressed by Eq. 2:

$$\Delta(\gamma^{SG}S) = \Delta\gamma^{SG \to SS}S + \gamma^{SG}\Delta S, \qquad (2)$$

where γ^{SG} is the interfacial energy of the solid/gas interface (loose powder), $\Delta\gamma^{SG\rightarrow SS}$ is the change of the interfacial energy (γ^{SG}-γ^{SS}) of grain boundary formation (γ^{SS}) caused by sintering, S is the surface area of the initial powder and ΔS is the lowering of the surface area caused by particle coarsening. In Eq. 2 both members of the right side are negative, which means that the decrease of the surface energy of the system can be caused by both sintering and coarsening (illustrated in *Figure 7*) [3].

Unfortunately, coarsening and grain growth are undesirable effects in many applications because they degrade some important properties, such as hardness [27], flexural strength [28], resistance to wear [29, 30, 31], electric conductance along grain boundaries [32] or optical transparency [33, 34].

2.3.4 Mechanisms of Reduction of Interfacial Energies

When the powder particles are in the contact, curvature gradients are formed. Applied heat causes extensive atomic movement and through mass transport mechanisms these curvature gradients are eliminated and flatted. As shown in *Figure 8* there are two types of curvature [25]:
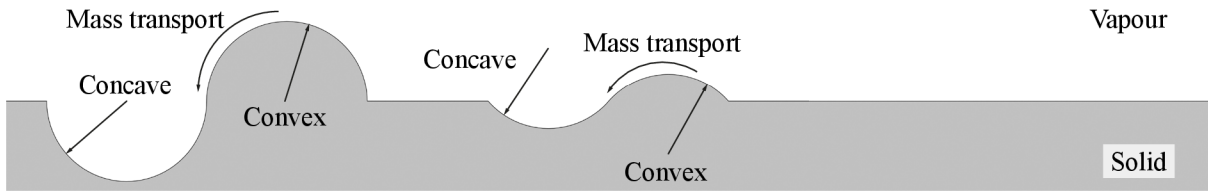
- Negative: the centre of curvature radius is outside the mass and the curvature is concave.
- Positive: the centre of curvature radius is inside the mass and the curvature is convex.

Figure 8: Change of surface curvature.

The concave surface is represented by vacancies and provides space where mass from convex surface will sink. The meaning of this transport, sinking the mass and flattering the surface, is to eliminate stress caused by the curvature regions. Flat surfaces are assumed to be stress-free, while convex surfaces are under tension of material atoms and concave surfaces are under compression. Hence, the saddle surface of the neck is mixture of both concave and convex curvatures [25].

The way of how to link stress σ and curvature represents the generalized Laplace relation (Eq. 3):

$$\sigma = \gamma\left(\frac{1}{r_1} + \frac{1}{r_2}\right),\qquad(3)$$

where r_1 and r_2 are the radii of arcs on a surface and γ is the surface energy [25].

2.3.5 Effects of Grain Boundaries

The presence of grain boundaries in polycrystalline materials dictates the equilibrium shapes of the pores and the grains. As illustrated in *Figure 9*, pore surrounded by three grains, there have to be an equilibrium among forces of surface tension. These forces are represented by surface energies of interfaces. The balance of forces leads to Eq. 4, where ψ is the dihedral angle:

$$\gamma_{SS} = 2\gamma_{SG}\cos\frac{\psi}{2}.\qquad(4)$$

One of the important consequences of the presence of grain boundaries is that grain

growth provides an alternative process by which the powder system can decrease its energy (by reducing the total grain boundary energy). This overall process is described as coarsening. Coarsening therefore occurs concurrently with sintering [35].
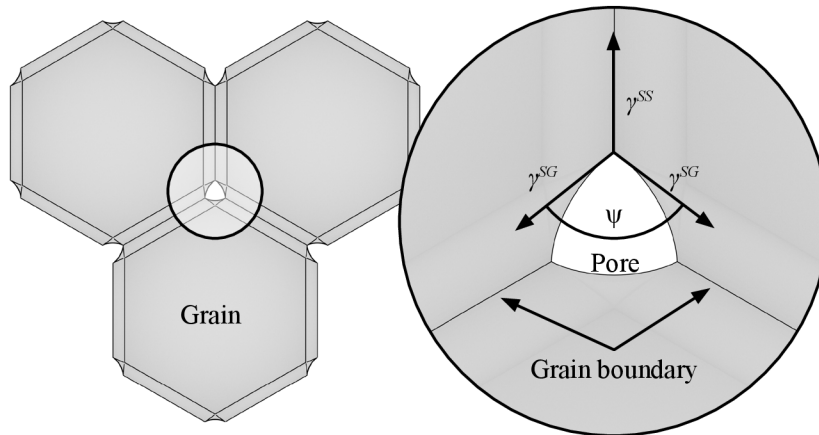
Figure 9: Illustration of dihedral angle in three grain junction.

2.3.6 Mechanisms of Mass Transport

Transport mechanisms determine how mass flows in response to the driving force for sintering. In general, there are various types of mechanisms of mass transport with different sources of mass and different ways of transport, but only one target - neck. It depends on source of transport mechanism whether it participate on densification or not.
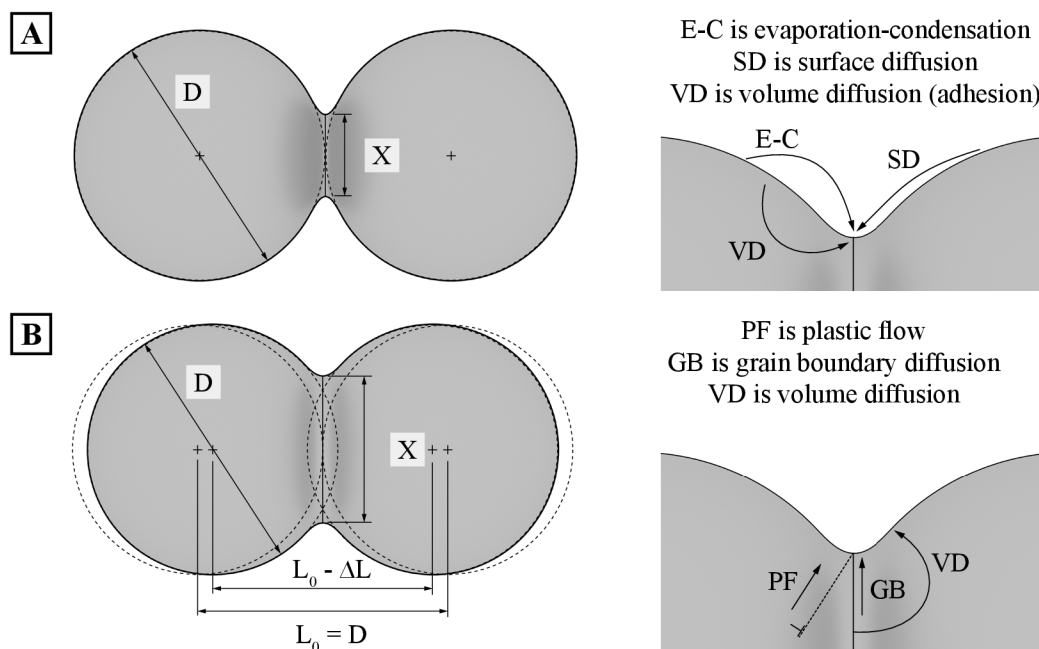
Figure 10: Mass transport mechanisms. A) illustrates surface transport (without densification) and B) illustrates bulk transport (with densification). D and X are dimensions characteristic for neck.

When source of mass transport originates from surface of particle (*Figure 10A*), surface diffusion, evaporation-condensation and volume diffusion provide ways to accumulate mass on neck. These mechanisms are relatively unwanted, because they flatten neck curvature and retard sintering speed. On the other hand, when source of mass transport originates from volume of

particle (*Figure 10B*), grain boundary diffusion and lattice diffusion transport mass to neck. These mechanism provides densification (particle centres converge) and they are positive for sintering process.

Mass flow is represented as vacancy and atom exchanges, where the atoms move along particle surfaces (surface diffusion), across pore spaces (evaporation-condensation), along grain boundaries (grain boundary diffusion), and through the lattice interior (viscous flow or volume diffusion). Also, the dislocation structure plays role in plastic flow and dislocation climb. Additionally, vacancies migrate between pores, leading to the growth of larger pores while the smaller pores shrink [25].

Surface Diffusion

Even if surface might appear smooth, at the atomic scale it is quite defective. On the surface of crystal solid, numerous defects are present, such as extra atoms, surface vacancies, terraces, ledges and adsorbed atoms (*Figure 11*).

In a typical surface diffusion event, three steps are involved. In the first step, an atom breaks existing bonds, typically from a surface kink. Once dislodged, the atom tumbles across the pore surface via random motion. Finally, the atom attaches a new surface site, possibly again at a surface vacancy or kink. Since the atoms are only repositioning to create a smooth surface, there is no substantial centre motion between particles, and thus no shrinkage [25].
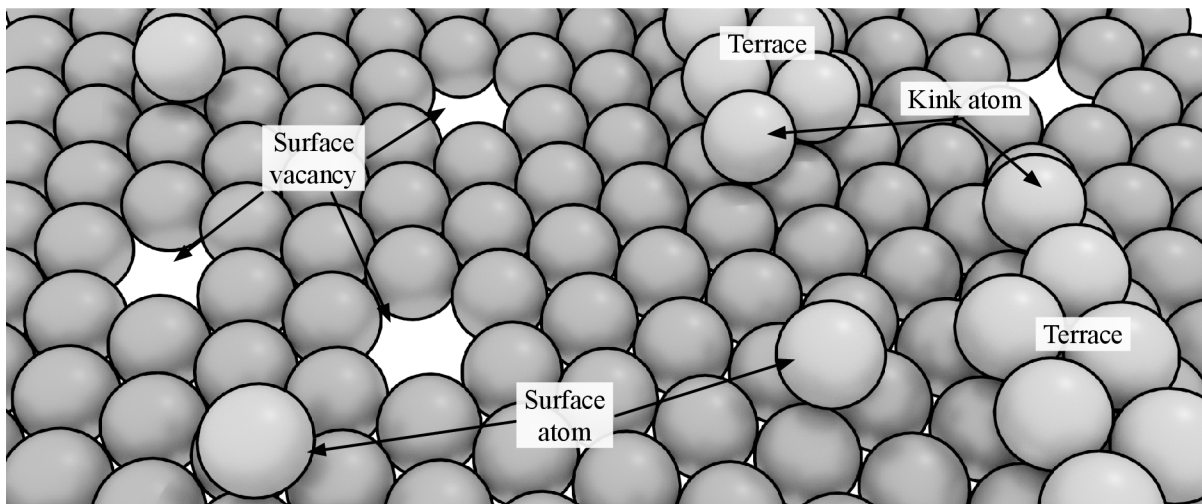
Figure 11: Surface flaws and imperfections of crystalline material surface.

Although atomic motion is random, atoms tend to migrate from convex to concave surfaces due to differences in defect concentrations. The result is a reduction in curvature and effective pore rounding. The neck between particles is particularly stressed, so is a preferred sink for atoms [25].

Surface diffusion is the most active during heating to the sintering temperature. The activation energy for surface diffusion is usually low compared to energy for other mass transport processes. Consequently, it initiates at lower temperatures and is dominant while there is a high surface area and little grain boundary area (the latter increases as interparticle bonds grow). As surface area is consumed, surface diffusion naturally declines in importance [25].

Volume (Lattice) Diffusion

In a crystalline material, volume diffusion (also called lattice diffusion) involves atoms exchange with vacancies. Applied heat induces atomic motion and causes atoms jump to vacancy places. At any temperature there is an equilibrium in population of vacancies. On the other hand, there is also a flow of vacancies between pores, leading to an increase in the median pore size as porosity decreases [25].
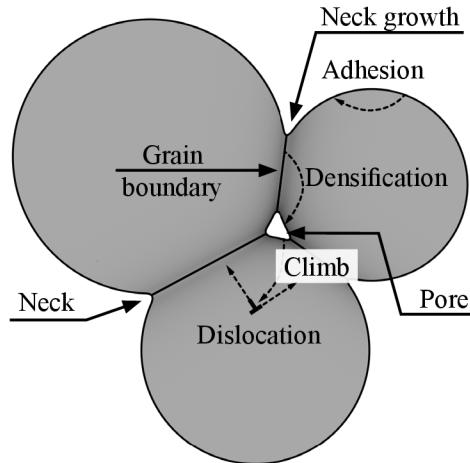
Figure 12: Various mechanisms of volume diffusion: adhesion (vacancy source and sink are the pore surface), densification (vacancy source is pore and sink is grain boundary) and dislocation climb (vacancy source is pore and sink is dislocation).

The motion of vacancies along certain paths is involved in volume diffusion illustrated in *Figure 12*. The primary mechanism is volume diffusion densification. It is a bulk transport process that involves vacancy flow to the interparticle grain boundary from the neck surface. Volume diffusion transports mass from the grain boundary to the pore, effectively moving vacancies from pores to annihilation at the defective region of the grain boundary. Densification and shrinkage occur since layers of atoms are removed along the particle contacts and repositioned on the pore surface. Consequently, the particle centres approach as the sinter bond grows [25].

Grain Boundary Diffusion

Grain boundary diffusion is important for sintering densification. Grain boundaries are formed within the neck between individual particles as a consequence of random grain contacts, leading to misaligned crystals. A grain boundary is essentially a collection of repeated misorientation steps. The defective character of the grain boundary allows mass flow along this interface with an activation energy that is usually intermediate between that for surface diffusion and volume diffusion [25].

Grain boundary diffusion depends on grain boundary area per unit volume. As surface area is consumed and surface diffusion declines in importance, the simultaneous emergence of new grain boundaries increases the role of grain boundary diffusion. Since the powder compacts are composed of large numbers of grain boundaries, it is reasonable to ignore differences in diffusion rates with orientation and assume average behaviour [25].

2.4 Pore Morphology Evolution in Sintering Process

2.4.1 Theory of Pore Closure

At the beginning there are spherical particles in contact and pore structure is all around. However, when compact is heated, contact points are transformed to grain boundaries, powder particles are turned to polyhedral grains and pore structures tend to stick on grain edges. Idealised grain structure for the second stage is a tetrakaidecahedron (*Figure 13A*) with tubular pores accommodated on grain edges (*Figure 13B*) [36].
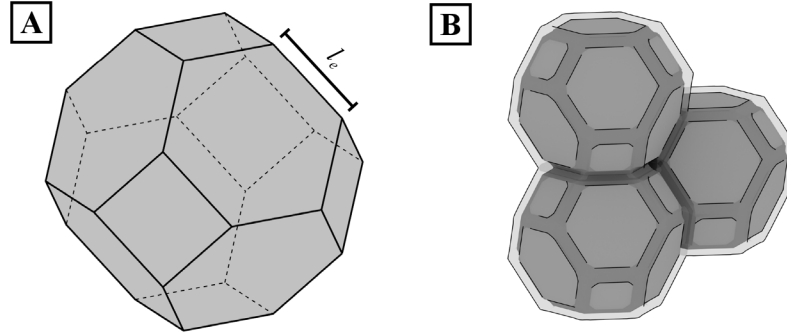
Figure 13: A) Illustration of tetrakaidecahedron (truncated octahedron) geometry B) Tetrakaidecahedron grains in compact with tubular pores situated on grain edges.

Tetrakaidecahedron (Truncated octahedron) is geometrical body with 36 edges, 14 faces (6 squares and 8 hexagonal) and volume (V_{TKDH}) dependent on the length of edge l_e (Eq. 5):

$$V_{TKDH} = 11.3 l_e^3. \qquad (5)$$

The formation and shape of pore phase is determined by dihedral angle and therefore by surface energies as mentioned in previous chapter 2.3.5. Since grain boundary energies are usually less than half of the surface energy of the material under consideration, the dihedral angle of pore is high. Therefore pore could be considered to be cylindrical for simple models, such as Budworth's geometrical model [36].

As temperature is rising, those tunnel-like structures pinch off and isolated pores are formed. In general, conditions for closure of tubular phase are known as Rayleigh's criterion [37], which suggests that infinitely long cylindrical pore channels are unstable to axial (longitudinal) perturbations with wavelength λ_{crit} exceeding the cylinder circumference $2\pi r_c$.

2.4.2 Rayleigh Instability

Rayleigh instability is a phenomena firstly described on fluid jets, for example from a water tap or a shower head. Basically it is the transformation of long cylindrical tube to spherical droplets due to decreasing surface energy. The thermodynamic condition to break-up the cylindrical tube is exceeding critical wavelength λ_{crit}, which causes amplitude of infinitesimal perturbations (in pore structure, always present due to flaws in pore surface) to increase. Increasing amplitude of perturbations will increase the curvature gradients on surface of the cylinder and therefore will provide the driving force to break-up the cylinder. There is a certain condition for determining which perturbation will take part in transformation. In an isotropic system, infinitesimal perturbations with wavelength $\lambda_- < 2\pi r_c$ (r_c is the cylinder radius) are predicted to decay, which keep pores stable and eventually cause pore to form one sphere (spheroidization [38]). On the other hand, perturbations with a wavelength $\lambda_+ > 2\pi r_c$ increase in amplitude and transform cylinder to numerous spheres (ovulation [38]).

Nichols and Mullins [39] extended this method and evaluated the conditions for solid cylindrical rods and for the breakup of cylindrical voids in a solid via surface or lattice diffusion.

In sintering practice ovulation (*Figure 14A*) is desired form of transformation because occurs at high densities (r_c is relatively low and decreases, while l_e is nearly constant) and controls grain growth. On the other hand, spheroidization (*Figure 14B*) occurs at low densities (r_c is relatively high and decreases, while l_e is nearly constant) and does not provide grain growth control. Evidence of such behaviour can be found in the final stage of sintering, where spherical pores are situated on grain junctions.
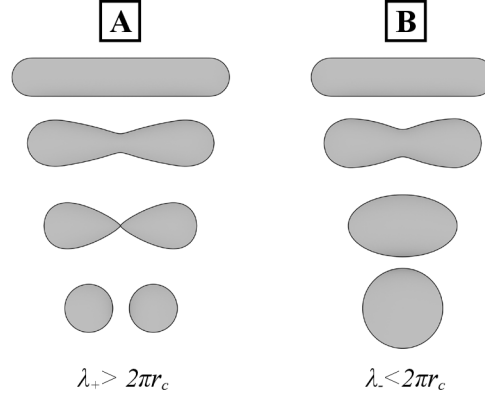
Figure 14: Illustration of tubular pore break up. A) ovulation, B) spheroidization.

2.4.3 Budworth's Model

Budworth's model presents a simple theory of pore closure during sintering. The whole idea is based on idealised polyhedral grain structure composed of tetrakaidecahedrons and idealised tubular pore structure situated on grain edges. Pore structure is idealised because of its geometry, which is assumed to be tubular. Cylinder (radius r_c, length l_c) attached on the edge will cause dihedral angle to be 180°. Which means by Eq. 4 that interfacial energy γ^{SS} will be equal to zero as illustrated in *Figure 15*.
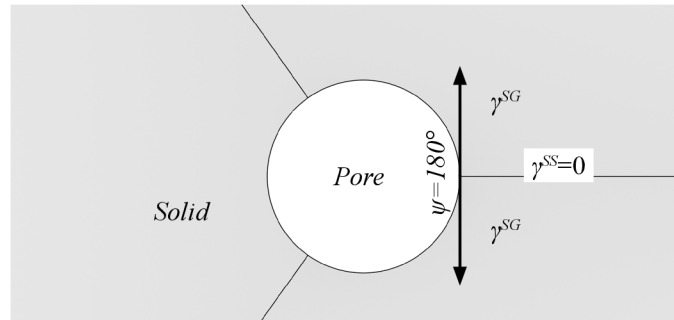
Figure 15: Dihedral angle and interfacial energies in Budworth's model.

With these assumptions and Rayleigh instability criterion, one could observe combination of parameters which will determine critical porosity P_{crit} (Eq. 6) when tubular pores will no longer be stable.

$$P_{crit} = \frac{12 \cdot V_{Pcrit}}{V_{Gcrit}}, \qquad (6)$$

$$V_{Pcrit} = \pi r_c^2 l_{Pcrit}, \qquad (7)$$

$$V_{Gcrit} = 11.3 \cdot l_{Gcrit}^3 = 11.3 \cdot l_{Pcrit}^3, \qquad (8)$$

14

where 12 is number of edges of tetrakaidecahedron in compact, V_{Pcrit} (Eq. 7) is critical volume of porosity, $l_{Pcrit}=2\pi r_c$ is critical pore length, V_{Gcrit} (Eq. 8) is volume of grain with edge length $l_{Gcrit}=l_{Pcrit}$.

The value of critical porosity from Eq. 9 , which is equal to relative density value of 91.55%.

$$P_{crit} = \frac{12 \cdot \pi r_c^2 l_{Pcrit}}{11.3 \cdot l_{Pcrit}^3} = \frac{12 \cdot \pi r_c^2}{11.3 \cdot l_{Pcrit}^2} = \frac{12 \cdot \pi r_c^2}{11.3 \cdot (2\pi r_c)^2} = \frac{3}{11.3 \cdot \pi} = 0.0845 \rightarrow 8.45\%. \qquad (9)$$

This value can be considered to be the lowest possible critical relative density for idealised grain structure.

2.4.4 Beere's Model

Beere's calculations present a model of grain edge porosity covering a wide range of surface to grain energy ratios (for various dihedral angles, various materials). The model is based on energy considerations and predicts shapes, surface curvature and stability of pores. The geometry of pore structure is no longer mere cylinder, but porosity has complex anticlastic or synclastic curvature. Unfortunately, whole model is not as simple to present with all its equations as Budworth's model, so step-by-step calculations will not be shown, although they can be found in [40].

This theory is based on equilibrium shape of pore found from consideration of its free energy. Calculated equilibrium shape for a particular volume fraction, surface energy and grain boundary energy is then the same whether the shape is gas filled, liquid filled or empty. This statement is true in real situations when the change in volume takes place slowly with rapid surface accommodation, which means that the surface curvature is the same everywhere and the dihedral angle at the boundary is a constant. Assumption like this is necessary to make the problem traceable and is adequate for many high temperature processes [40].

The equilibrium shape of grain edge pores is calculated by considering the porosity to be accommodated on the edge of an idealized tetrakaidecahedron and the energy calculations are based on a unit of porosity situated on a grain corner (*Figure 16*) [40].
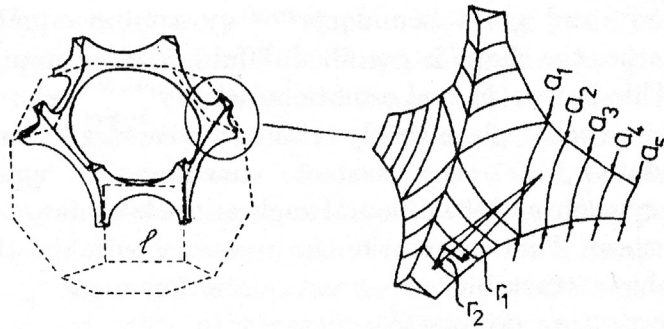
Figure 16: An idealised system of porosity situated on the edges of a tetrakaidecahedron grain [40]

The minimum energy of the configuration is found by computer calculation by setting the volume of unit porosity as fixed. Dimensions of the pore unit a_1-a_4 (from *Figure 16*) undergo small additions and subtractions recalculating dimension a_5 to maintain a constant volume. The goal of this process is to find energy minimum for given volume. The procedure is repeated for different volume fractions and different surface to grain boundary energy ratios [40].

Figure 17 shows the calculated shape of open pores when porosity is 10% of volume.

The dihedral angle is 180° (same situation as in Budworth's model), which causes that interfacial energy of grains converges to zero. The pores have rounded shape and the section connecting the corners collapses when porosity fraction is reduced below about 8% [40].

Previous calculations discover the minimum energy for particular volume, which is the energy of a pore with surfaces everywhere at equilibrium. However, pore may not be at equilibrium with respect to the change in volume. The tendency to shrink or grow may be found by considering the change in minimum energy with volume change. Therefore additional calculations have to be made [40].
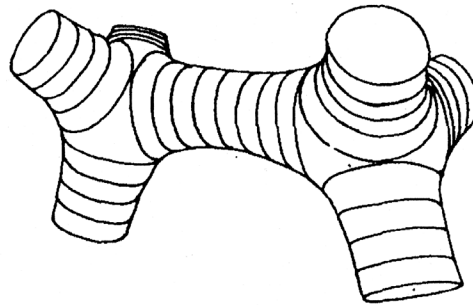
Figure 17: Predicted shape of 10% porosity volume fraction created by two adjacent corner units when the dihedral angle is 180° [40].

Final output from this model is following dependency of critical porosity on dihedral angle (*Figure 18*). There are two limiting values of dihedral angle: the first is 180° corresponding with 8% critical porosity and the second is 60° corresponding with 0% critical porosity. 60° dihedral angle enables the pore structure to form equilateral triangle (in cross-section) and be stable for any length.
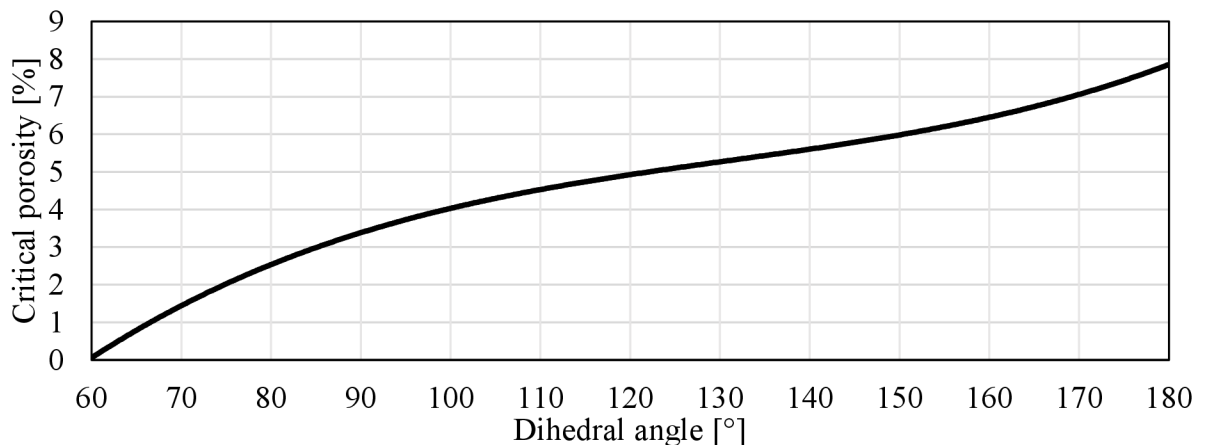
Figure 18: Final output of Beere's model considering energetic minimum with respect to a volume and a surface equilibrium.

2.4.5 Carter's & Glaeser's Model

This model [41] is focused on application of Ryleigh instability to intermediate stage of sintering considering thermodynamic condition for break up of tubular pore channels along n-grain junctions as a function of dihedral angle. For the purpose of this diploma thesis, *n* (number of grains surrounding pore) will be set to *n=3*, which refers to three grain junction used in Budworth's and Beere's models. Alike the previous model, the calculations are quite complicated, therefore they will not be described step-by-step, nor will every equation be shown in full form. However, whole calculation process can be found in [41].
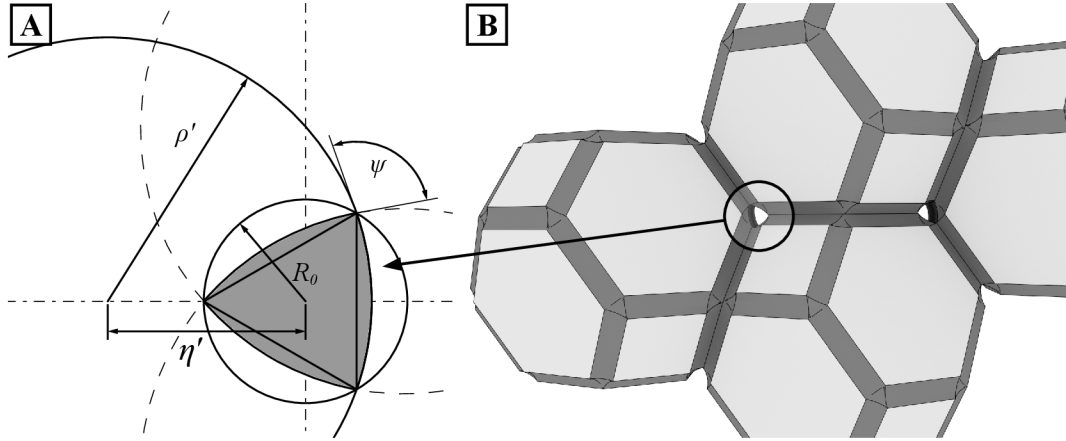
Figure 19: A) Geometry of idealised three-sided pores.
Grey area corresponds to pore cross section [41].
B) Idealised grain compact composed of tetrakaidecahedrons.

The size of a symmetrical three-sided pore channel is described by a radius R_0 of a circle circumscribing the equilateral triangle formed by joining the three grain-boundary pore junctions (*Figure 19*). This geometry is expected to be suitable for material with isotropic grain boundary and surface energies (which means a constant dihedral angle). Another condition to make this model work is assumption of constancy of chemical potential on the pore surface which requires constant curvature. Therefore, each side of the pore in two dimensions must then be a circular arc of radius $\rho' = \rho R_0$ having an origin at a distance $\eta' = \eta R_0$ from the pore centre [41]. Both parameters of pore geometry is function of dihedral angle ψ as can be seen from Eq. 10 and Eq. 11:

$$\rho = -\sin\frac{\pi}{3} \cdot \sec\left(\frac{\pi}{3} + \frac{\psi}{2}\right), \qquad (10)$$

$$\eta = -\cos\frac{\psi}{2} \cdot \sec\left(\frac{\pi}{3} + \frac{\psi}{2}\right). \qquad (11)$$

The goal of the calculations is determination of a condition when perturbations with wavelengths bigger than λ_{crit} will increase in amplitude (only these perturbations decrease the average surface area per unit length, or equivalently, the average energy per unit volume). Such a requirement represents Eq. 12:

$$\lambda_{crit} = 2\pi R_0 \cdot \left(\frac{P}{U - 2\cos\frac{\psi}{2}}\right)^{\frac{1}{2}}. \qquad (12)$$

The dihedral angle dependence of λ_{crit} thus determines perturbations capable of producing the transition from continuous to closed porosity [41]. Where U (Eq. 13) and P (Eq. 14):

$$U = 2\rho\left(\frac{\psi}{2} - \frac{\pi}{6}\right),\qquad(13)$$

$$P = (2\rho^3 + \rho\eta^2)\left(\frac{\pi}{3} + \frac{\psi}{2} - \frac{\pi}{2}\right) +$$

$$+ \cos\frac{\psi}{2}\left(5\eta\rho^2\cos\frac{\pi}{3} - 2\eta^3\sin^2\frac{\pi}{3}\cdot\cos\frac{\pi}{3} - \eta^2\rho\sin\frac{\psi}{2} - 2\rho^3\sin\frac{\psi}{2} - 2\rho^3\sin^3\frac{\psi}{2}\right),\qquad(14)$$

are geometrical factors.

Dependency of critical porosity on dihedral angle can be created using similar calculations as in Budworth's model, assuming the tetrakaidecahedron as a grain shape with edge length equal to λ_{crit} and substituting into Eq. 9 as $\lambda_{crit} = l_{Gcrit} = l_{Pcrit}$. Decreasing stability of pore channels with change of dihedral angle is shown in *Figure 20*.
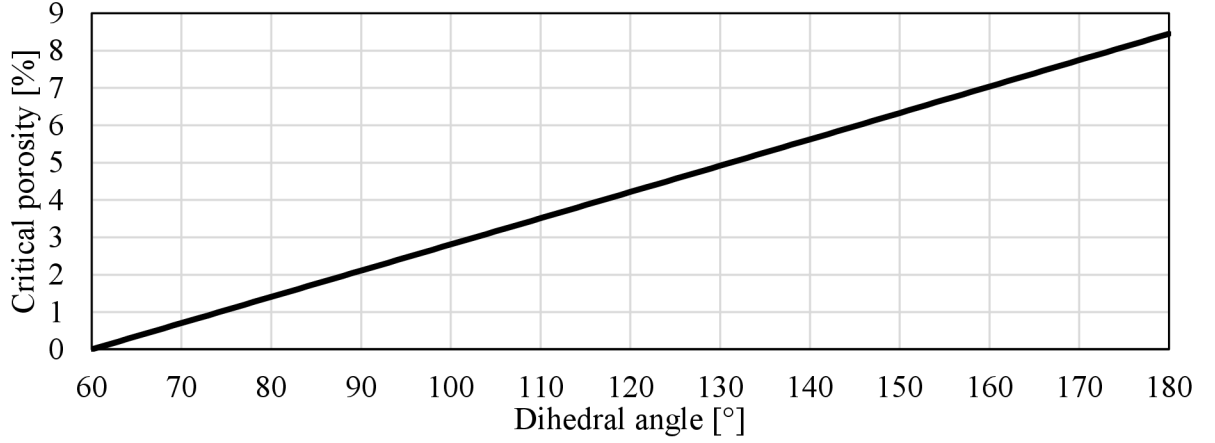
Figure 20: Effect of dihedral angle on stability of continuous phase in Carter's & Glaeser's model.

2.5 Pore Elimination

The main goal in majority of ceramics manufacturing processes is to achieve 100% theoretical density. However, this ambition is hard to fulfil only with elevated temperature due to additional conditions for microstructure, chemical, biological, mechanical, optical properties of final ceramic product. Those properties are often connected with grain size. As it was mentioned in previous chapters, in the second stage of sintering pore structure is accommodated on grain edges thus inhibits grain growth (coarsening) effect [42]. In the third stage pore structures break up to spherical or lenticular shape situated (in ideal case of Coble's model [26]) on grain corners (*Figure 21*) and initiate the unrestricted grain growth.
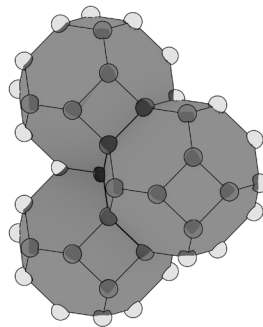
Figure 21: Idealised model of grains for the third stage of sintering with spherical pores on grain corners.

2.5.1 Condition for Pore Shrinkage

At the final stage of sintering, where the pore size is usually smaller than the grain size, the pore shape, which is determined by the dihedral angle, is not the primary parameter by which microstructural development is analysed. In contrast, for pores of size comparable to or larger than the grain size, pore shape is an important parameter. Depending on the dihedral angle and ratio of pore size to grain size, pores cannot shrink unless a critical condition is satisfied as a result of grain growth [7].
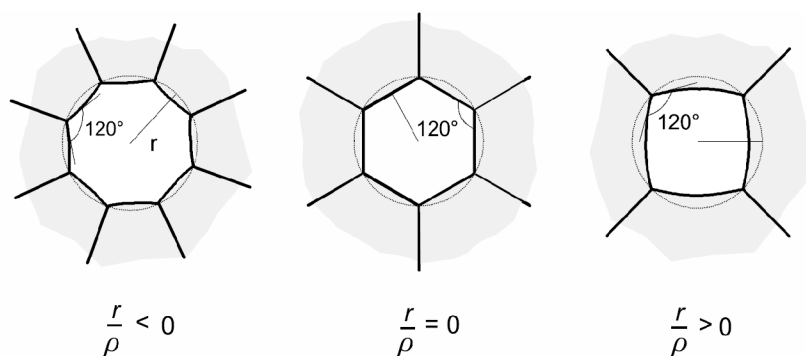
Figure 22: Illustration of pore behaviour change with number of grain neighbours [7].

Such a critical condition was postulated by Kingery and Francois [43] by calculating the critical number of grains surrounding a pore required to make the grain surface flat for a given dihedral angle. *Figure 22* illustrates three types of surface curvature associated with various numbers of grains n for a 2D system and a dihedral angle of 120° (for illustrative purpose, in reality dihedral angle might be different for the material under present conditions). In this case the ratio of pore radius r to surface curvature radius ρ varies from negative (when

$n>6$), through zero (when $n=6$), to positive (when $n<6$). For negative ratio the grain boundary is convex and the chemical potential of atoms at the grain surface is higher than at the grain boundary and thus pore has a tendency to expand. On the other hand, for a grain number less than six, the pore tends to shrink. For a two-dimensional structure, the condition for pore shrinkage can be found in Eq. 15:

$$\psi > \left(1 - \frac{2}{n}\right)\pi, \qquad (15)$$

where ψ is dihedral angle and n represents number of surrounding grains [7].

2.5.2 Pore Separation from Grain boundaries

When pores are situated on grain boundaries, vacancies can move (via curvature gradients, decreasing of interfacial energy and diffusion) and thus pores can be removed by sintering or hot isostatic pressing. However, when pore separates from grain boundary, the pore is entrapped in grain and cannot be easily eliminated [44]. Therefore, pore/boundary separation represents the limit of densification in sintering. Separation occurs when the boundary migration velocity is higher than pore migration velocity.

For pore/boundary separation there are two extreme cases that can be considered:
- Mobility of pore is lower than mobility of grain boundary ($M_P < M_{GB}$).
- Mobility of pore is bigger than mobility of grain boundary ($M_P > M_{GB}$).

The first case corresponds to a system with a high number of large pores at the beginning of final stage of sintering. However, as densification proceeds, the inhibition force of pores against boundary migration decreases and separation can occur [7]. On the contrary, the second case is valid for a system having a small amount of highly mobile pores and grain boundaries with low velocities. When grain growth occurs and the boundary migration velocity becomes slow, the separated pores can reattach and keep up with the moving boundary. Until this condition is satisfied pores are separated [7].

From informations above one can assume ideal sintering cycles to achieve ideal microstructure and theoretical density of sintered material. The ideal sintering cycle should provide minimal coarsening during intermediate stage (via pores on the grain edges blocking grain growth) and do not let grain boundaries absorb pores. Next process is to eliminate remaining porosity via lowering temperature and elongation sintering time (two-step sintering) or via any kind of pressure assisted sintering.

2.6 Hot Isostatic Press (HIP)

Hot isostatic pressing is sintering technique, which combines gas pressure (widely used inert argon) and elevated temperature (*Figure 23*). Used gas as pressure agent require sample with closed pores to eliminate gas flow through the specimen. If gas becomes entrapped in the pores and the gas pressure is increased during pore shrinkage, the densification process can be slowed down, or even stopped entirely. Moreover, such open pores cannot be eliminated by sintering with high gas pressure if entrapped gas is insoluble in the material [45].
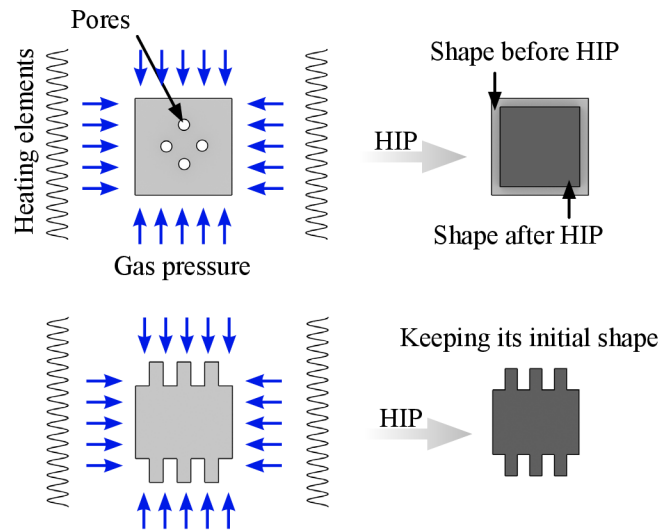
Figure 23: Illustration of hot isostatic pressing principles.

HIP is successfully used as final step in process of creating fully dense ceramic samples with small grain size. Green body is sintered in order to obtain a dense surface (without open porosity) and to apply the gas pressure afterwards (principle is shown in *Figure 24*), which can be manage in two ways. One approach is to sinter material to close porosity stage in a single step and then hot isostatic press is a second step, often in a separate sintering furnace (post-HIP). Approach number two consists of a two-step sintering process in which a closed porosity is obtained at low or no gas pressure during the first sintering step and full density is achieved during a subsequent HIP step with maximum gas pressure in the same furnace (sinter-HIP) [45].
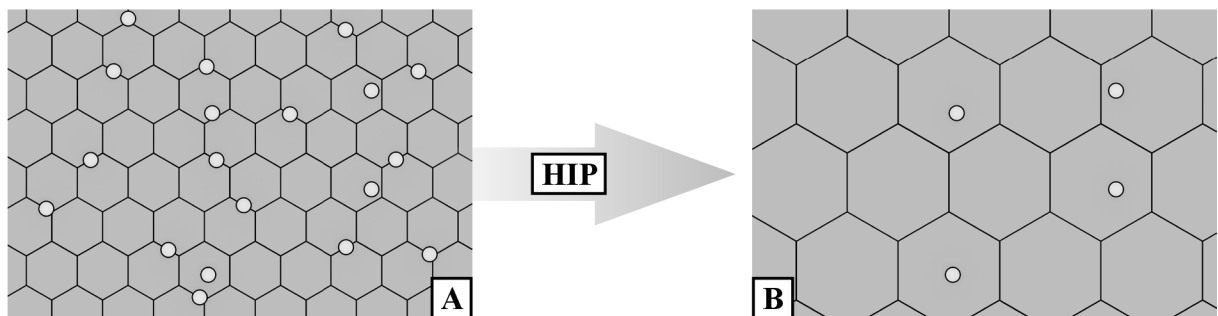
Figure 24: Microstructure model for pore elimination by HIP. A) and B) represent material with closed pores attached to grain boundaries and pore elimination after HIP.

2.6.1 Applications of post-HIP process

Post-HIP processing technique is widely used to produce transparent products from various ceramic materials. In context of this diploma thesis only materials used in experimental part were chosen in this review part.

Alumina

Al_2O_3 with its mechanical strength, hardness, bioinertness and corrosive resistance is suitable candidate for transparent ceramic armour, bioceramics, electromagnetic windows or envelopes for high-pressure halide lamps [46]. Mechanical and optical properties of alumina ceramics are highly dependent on their grain size and residual porosity, therefore post-HIP process is more than promising candidate to achieve ideal result.

Creation of alumina transparent ceramics at BUT [47] is exceptional example of usability of post-HIPing procedure as final step of technological process. Zirconia-doped alumina disc was prepared by pressureless presintering followed by hot isostatic pressing with an in-line transmission of up to 70.4% at a wavelength of 632.8 nm and with a theoretical maximum in the infrared wavelength range between 2000 and 4000 nm, at a sample thickness of 0.8 mm was obtained [47].

Figure 25: Transparent zirconia-doped TM-DAR + Z(24) disc (80 mm diameter and 0.8 mm thickness) [47].

Zirconia

ZrO_2 ceramics posses exceptional mechanical and functional properties, such as high toughness, high oxygen diffusivity and low thermal conductivity. Unfortunately, pure ZrO_2 is very complicate to manufacture because of lattice (martensite-like) transformations which cause cracks during cooling after sintering. Therefore, stabilization (for example) by Y_2O_3 has to take place, this secure lattice configuration during sintering and produce yttria stabilized zirconia (YSZ). Stabilized zirconia can be divided by amount doped Y_2O_3 to tetragonal (3mol% Y_2O_3) or cubic (8mol% Y_2O_3), respectively. Tertagonal zirconia is used as material for bioinert replacements of joints, mainly because of possibility to increase toughness and ability to stop cracks via transformation mechanism with volume increasing (tetragonal lattice to monoclinic lattice). Cubic zirconia is attractive by unique combination of mechanical and optical properties [48].

Again experiments of validity of post-HIP as ideal procedure for removing porosity can be mentioned: IR transparent tetragonal zirconia [33] and transparent cubic zirconia [49].

Spinel

MgAl$_2$O$_4$ ceramics posses polycrystalline structure which is optically isotropic and transparent to electromagnetic radiation from the ultraviolet through the mid-infrared (0.2-5.5 μm) [46]. With high strength spinel is attractive material for manufacturing high performance components, such as lenses, IR windows and domes, protective windows for aircraft, ship and submarine IR sensors, etc.

Processing of transparent MgAl$_2$O$_4$ at BUT [50] can be highlighted as an real example of availability of post-HIPing procedure for pore elimination. Ceramic discs presintered to the lowest density value still guaranteeing the structure with closed porosity (94.9% t.d.) could be hot isostatically pressed at 1500 °C and 200 MPa to full density with an average grain size of 1 μm, real in-line transmission of 60% and Vickers hardness of 13 GPa [50].

Figure 26: The optical transparency of spinel ceramics (thickness 1.1mm) prepared with different presintered densities (from left: 94.9, 97.9 and 99.5 %t.d.). In the upper image the samples are lying immediately on the sheet of paper bearing the text; in the lower one they are 5 cm above it [50].

The different transparency is explained by authors: "The main reason for this behaviour could be trapping of pores in the grain interior due to extensive grain growth during excessive presintering. Such intragrain pores, trapped during presintering, remained even after the HIP." [50].

3   EXPERIMENTAL PART

3.1 Ceramic Materials

5 different ceramic materials were used for experiments performed in this master's thesis. These materials have different crystallographic structures and different particle size. Totally 9 ceramic powders were used for experiments. The details of these ceramic materials, including their particle size, are given in *Table 1*.

Table 1: Characterization of used ceramic powders

Material	Lattice	Powder type	Producer	Particle size [μm]	Label	T.D. [g/cm³]
Al_2O_3	Hexagonal	AKP 30	Sumitomo Chemical America Inc., USA	0.300	AKP	3.99
Al_2O_3	Hexagonal	Reynolds	Malakoff Industries, USA	0.240	REY	3.99
Al_2O_3	Hexagonal	Taimicron	Taimei Chemicals CO.,LTD, Japan	0.100	TAI	3.99
ZrO_2 doped 3mol% Y_2O_3	Tetragonal	TZ3Y	Tosoh, Japan	0.080	3Y	6.08
ZrO_2 doped 3mol% Y_2O_3	Tetragonal	TZ3YSB	Tosoh, Japan	0.140	3YSB	6.08
ZrO_2 doped 8mol% Y_2O_3	Cubic	TZ8Y	Tosoh, Japan	0.080	8Y	5.99
ZrO_2 doped 8mol% Y_2O_3	Cubic	TZ8YSB	Tosoh, Japan	0.140	8YSB	5.99
$MgAl_2O_4$	Cubic	Baikalox S30CR	Baikowski, France	0.058	S30CR	3.58

3.2 Shaping and Pre-sintering Process

Powders were formed by cold isostatic pressing using rubber moulds (*Figure 27A*) to bulk cylinder-like shapes (*Figure 27B*). Two different pressure values were used: for the first lot 100 MPa and for the second lot 300 MPa (both for 5 minutes), which caused different microstructure of the green body.
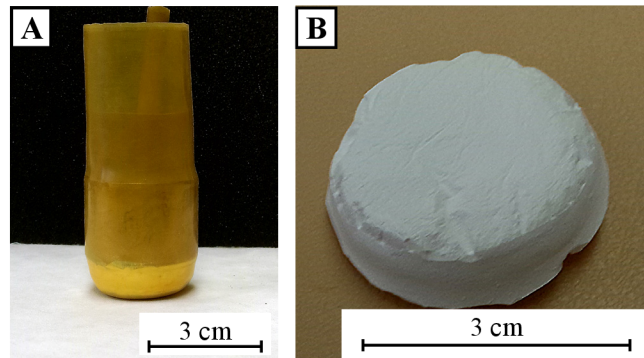
Figure 27: A) Rubber mould with powder inside, B) Pressed powder in disc shape, C) Disc cut into samples

After pressing green bodies were heated to 800 °C with 1hour dwell time to increase their manipulation strength and to remove binders. Subsequently discs were cut to smaller samples and polished on sand paper (polishing is not necessary, but provides better handling when measuring density).

3.3 Sintering Process

Samples were sintered in presureless Heraeus super-kanthal furnace (*Figure 28A*) at various temperatures to achieve volume of open pores (*Vo*) to be close to 0%. Sintering cycle (*Figure 29*) was composed of heating to 800 °C with 10 °C/min heating rate and heating to final temperature (*T*) with 5 °C/min heating rate, the cooling rate was 25 °C/min.
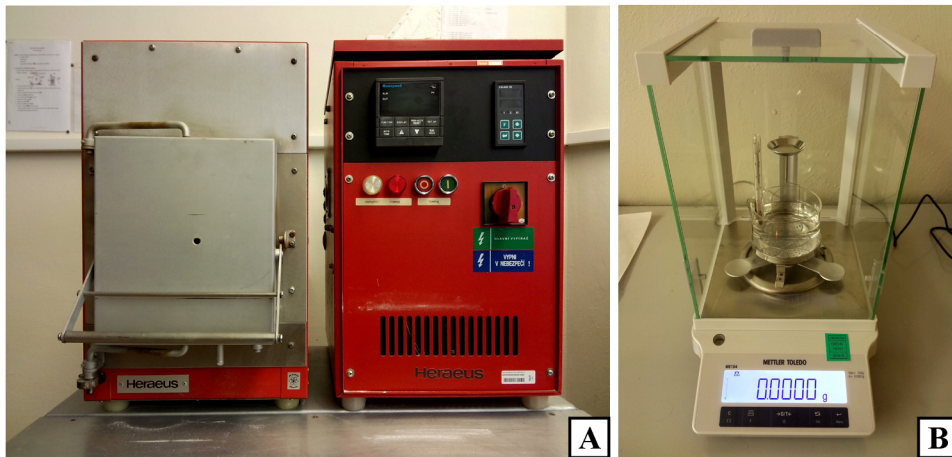
Figure 28: A) Heraeus super-kanthal furnace (Germany),
B) Mettler Toledo ME104 with density kit.
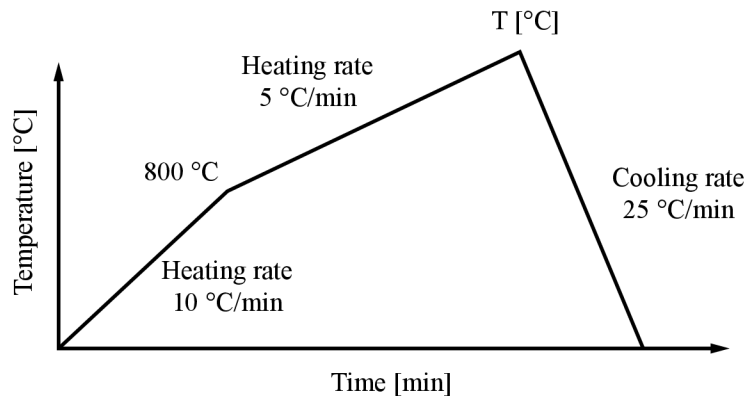
Figure 29: Illustration of sintering cycle.

3.4 Density Measurements

Density of sintered samples and ratio of open and closed porosity were measured by Archimedes method (EN 623-2) using analytic balances Mettler Toledo ME104 (*Figure 28B*) equipped with density kit with precision 0.1 mg by following procedure:
  • In the first step excessive wetness is removed from the samples by infrared lamp (approx. temperature is 110 °C) for 1 hour. After this, mass m_1 is measured. This value represents dry mass of the sample.

- In the second step air is removed from inside of the samples, via vacuum pump in exicator for 30 minutes.
- In the third step open porosity of the sample is flooded with distilled water with small amount of wetting agent in presence of vacuum, again for 30 minutes.
- In the fourth step air is let into the exicator and allow pressure in sample and surrounding pressure create equilibrium, same time as in previous step.
- In the fifth step mass m_2 is measured, which corresponds to mass of sample inserted to distilled water in density kit.
- In the sixth step mass m_3 is measured, which corresponds to mass of sample with dried surface, so only open pores are flooded.

$$\rho_{rel} = \frac{m_1}{m_3 - m_2} \cdot \frac{\rho_{H_2O}}{\rho_{teor}}, \qquad (16)$$

$$V_O = \frac{m_3 - m_1}{m_3 - m_2} \cdot 100 \, [\%], \qquad (17)$$

$$V_C = \left(\frac{m_1 - m_2}{m_3 - m_2} \cdot 100 \right) - \rho_{rel} \, [\%]. \qquad (18)$$

With knowledge of theoretical density of materials (see *Table 1*), relative density (ρ_{rel}) can be calculated using Eq. 16, volume of open (V_o) and closed porosity (V_C) can be calculated using Eq. 17 and Eq. 18, eventually. Distilled water used in these measurements changes density dependently on temperature ($T_{H_2O} \, [°C]$). This dependence was described by Eq. 19:

$$\rho_{H_2O} = \left(\frac{0.997 - 0.9984}{5 \cdot (T_{H_2O} - 20)} \right) + 0.9984 \, [kg \cdot m^{-3}] \qquad (19)$$

4 RESULTS

4.1 Results of Sintering of Alumina Powders

4.1.1 Porosity Change with Relative Density for AKP

Results of density, open and closed porosity measurements for Al_2O_3 AKP powder CIPed at 100 MPa and 300 MPa are shown in *Figure 30*. Open porosity decreases with increasing density until it closes approximately at 94-94.5% t.d. (CIP 300 MPa) and at 94.5% t.d. (CIP 100 MPa). More details about individual experiments such as sintering temperature, values of density and porosity can be found in *Appendix 1-2*.
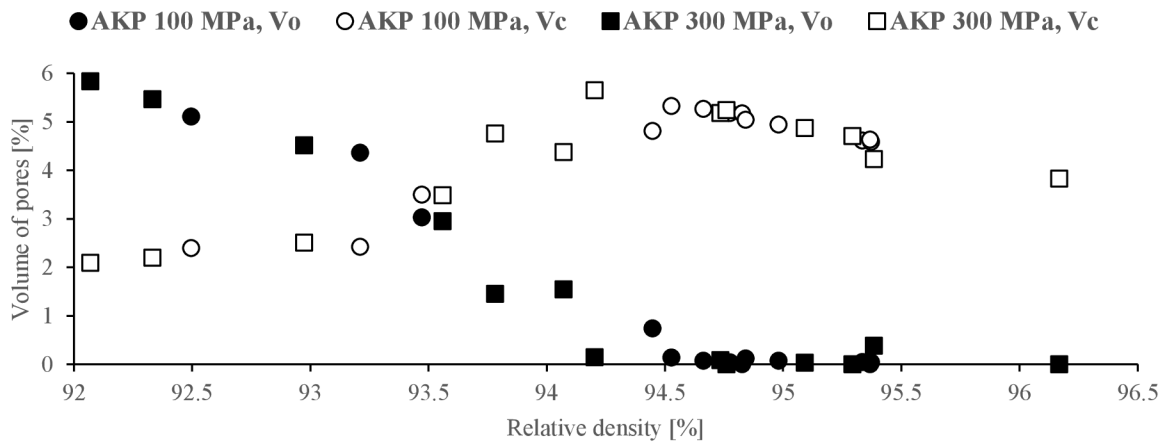
Figure 30: Evolution of porosity for AKP 100 MPa and 300 MPa CIP.

4.1.2 Porosity Change with Relative Density for REY

Results of density, open and closed porosity measurements for Al_2O_3 REY powder CIPed at 100 MPa and 300 MPa are shown in *Figure 31*. Open porosity decreases with increasing density until it closes approximately at 94.5% t.d. (CIP 300 MPa) and at 94.5% t.d. (CIP 100 MPa). More details about individual experiments such as sintering temperature, values of density and porosity can be found in *Appendix 3-4*.
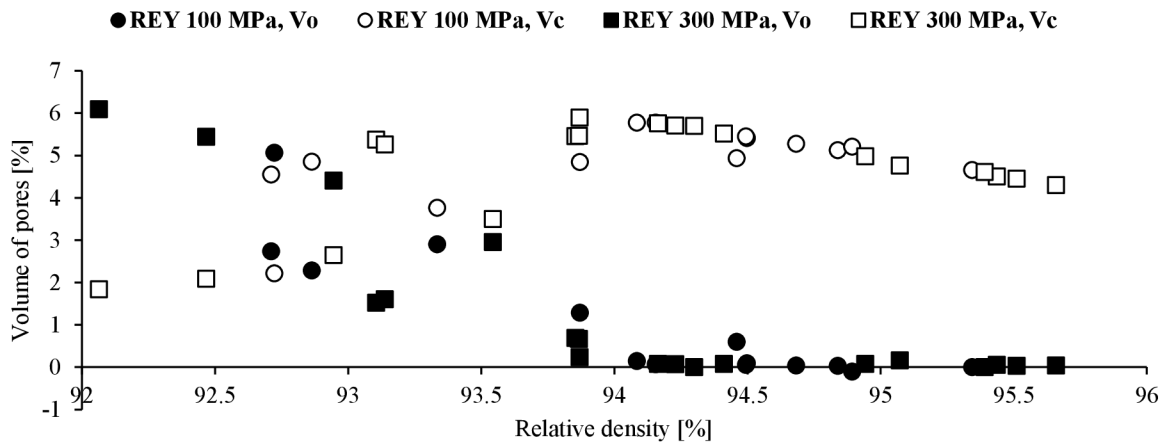
Figure 31: Evolution of porosity for REY 100 MPa and 300 MPa CIP.

4.1.3 Porosity Change with Relative Density for TAI

Results of density, open and closed porosity measurements for Al_2O_3 TAI powder CIPed at 100 MPa and 300 MPa are shown in *Figure 32*. Open porosity decreases with increasing density until it closes approximately at 96% t.d. (CIP 300 MPa) and at 95.5% t.d. (CIP 100 MPa). More details about individual experiments such as sintering temperature, values of density and porosity can be found in *Appendix 5-6*.
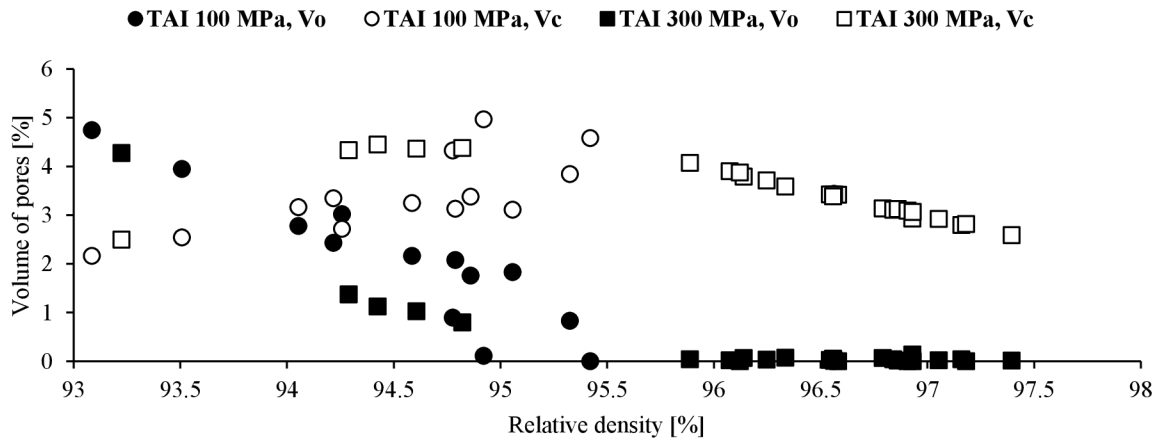
Figure 32: Evolution of porosity for TAI 100 MPa and 300 MPa CIP.

4.2 Results of Sintering of Spinel Powder (S30CR)

Results of density, open and closed porosity measurements for $MgAl_2O_4$ powder S30CR CIPed at 100 MPa and 300 MPa are shown in *Figure 33*. Open porosity decreases with increasing density until it closes approximately at 93.5% t.d. (CIP 300 MPa) and at 92.5% t.d. (CIP 100 MPa). More details about individual experiments such as sintering temperature, values of density and porosity can be found in *Appendix 7-8*.
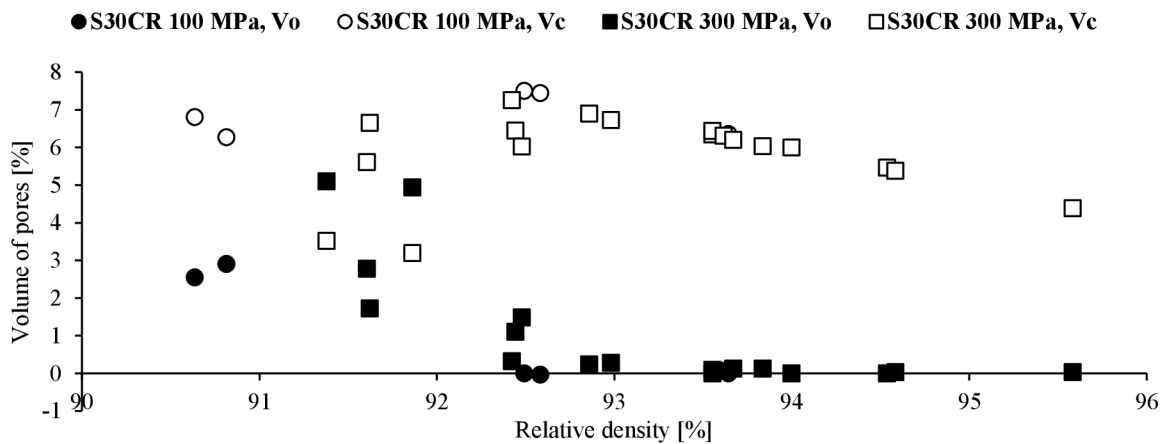
Figure 33: Evolution of porosity for S30CR 100 MPa and 300 MPa CIP.

4.3 Results of Sintering of Zirconia Powders

4.3.1 Porosity Change with Relative Density 3Y

Results of density, open and closed porosity measurements for ZrO_2 doped 3mol% Y_2O_3 powder 3Y CIPed at 100 MPa and 300 MPa are shown in *Figure 34*. Open porosity decreases with increasing density until it closes approximately at 92% t.d. (CIP 300 MPa) and at 93% t.d. (CIP 100 MPa). More details about individual experiments such as sintering temperature, values of density and porosity can be found in *Appendix 9-10*.
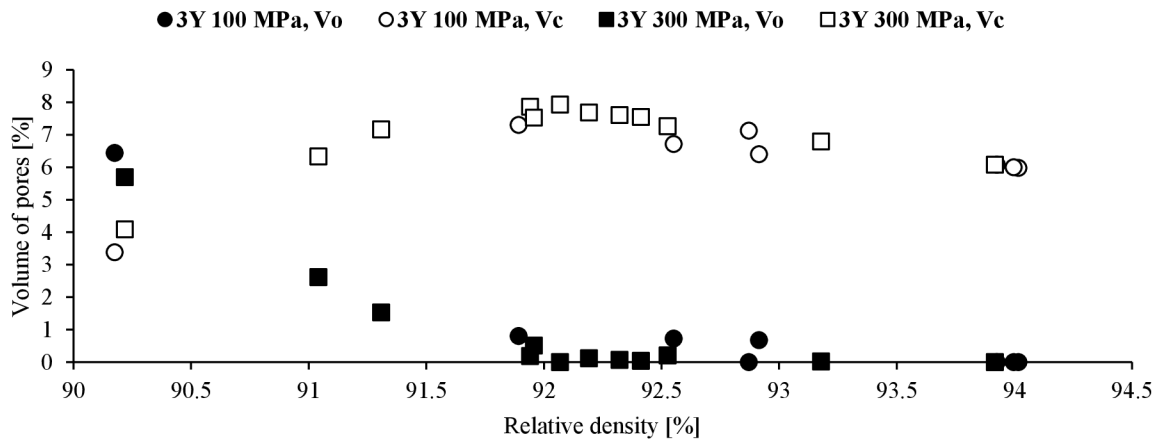
Figure 34: Evolution of porosity for 3Y 100 MPa and 300 MPa CIP.

4.3.2 Porosity Change with Relative Density for 3YSB

Results of density, open and closed porosity measurements for ZrO_2 doped 3mol% Y_2O_3 powder 3YSB CIPed at 100 MPa and 300 MPa are shown in *Figure 35*. Open porosity decreases with increasing density until it closes approximately at 94% t.d. (CIP 300 MPa) and at 93% t.d. (CIP 100 MPa). More details about individual experiments such as sintering temperature, values of densities and porosity can be found in *Appendix 11-12*.
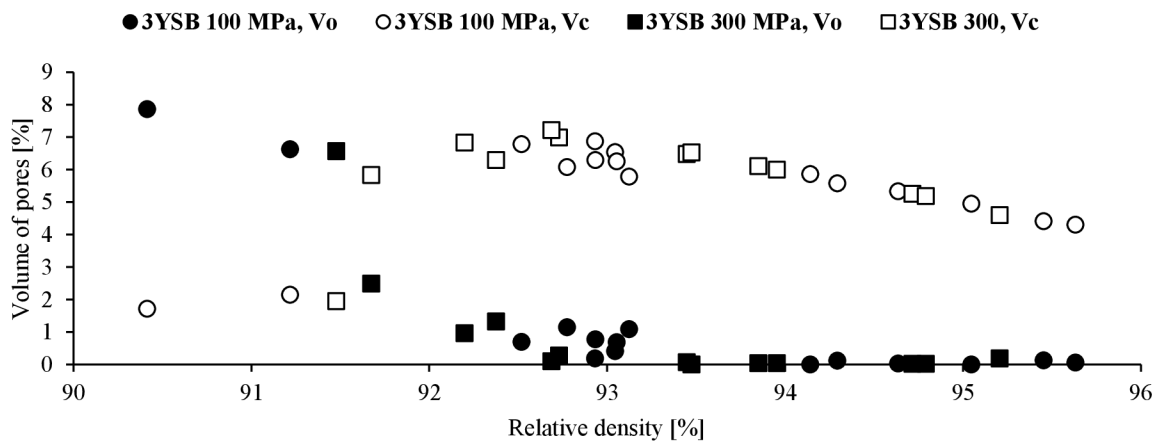
Figure 35: Evolution of porosity for 3YSB 100 MPa and 300 MPa CIP.

4.3.3 Porosity Change with Relative Density for 8Y

Results of density, open and closed porosity measurements for ZrO_2 doped 8mol% Y_2O_3 powder 8Y CIPed at 100 MPa and 300 MPa are shown in *Figure 36*. Open porosity decreases with increasing density until it closes approximately at 92% t.d. (CIP 300 MPa) and at 92% t.d. (CIP 100 MPa). More details about individual experiments such as sintering temperature, values of density and porosity can be found in *Appendix 13-14*.
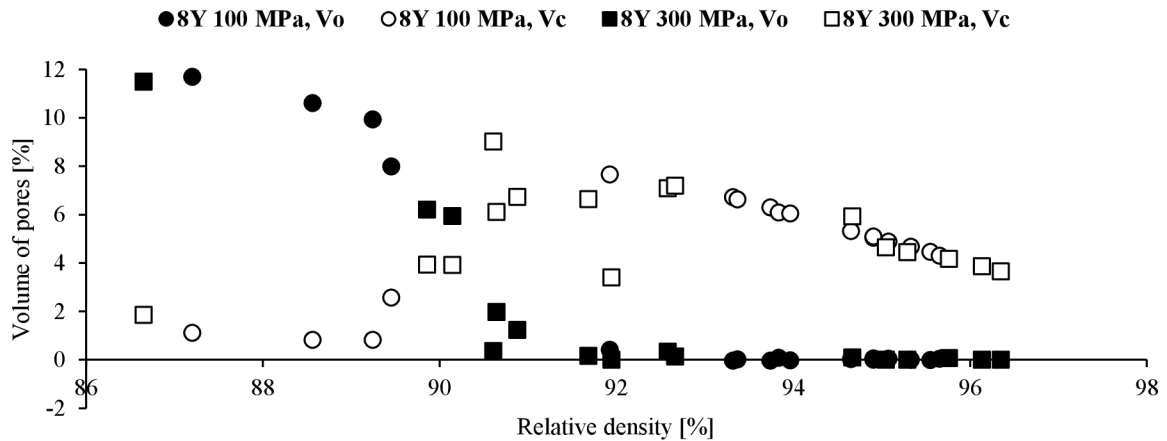
Figure 36: Evolution of porosity for 8Y 100 MPa and 300 MPa CIP.

4.3.4 Porosity Change with Relative Density for 8YSB

Results of density, open and closed porosity measurements for ZrO_2 doped 8mol% Y_2O_3 powder 8YSB CIPed at 100 MPa and 300 MPa are shown in *Figure 37*. Open porosity decreases with increasing density until it closes approximately at 93% t.d. (CIP 300 MPa) and at 93% t.d. (CIP 100 MPa). More details about individual experiments such as sintering temperature, values of density and porosity can be found in *Appendix 15-16*.
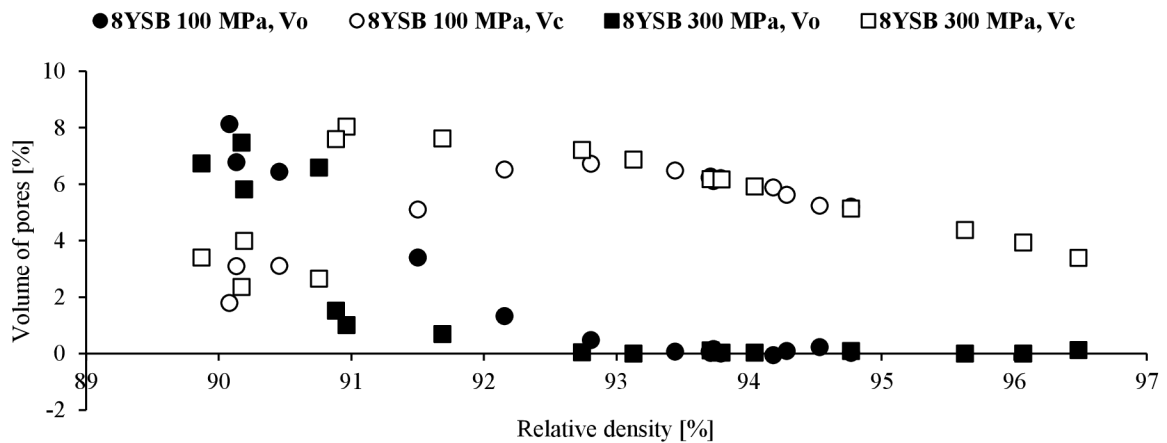
Figure 37: Evolution of porosity for 8YSB 100 MPa and 300 MPa CIP.

4.4 Summary of Results of Critical Density

Nearly critical relative densities (Vo ≤ 0.1%) of all used materials are shown in *Figure 38* and in *Table 2*. Values were taken from measured data (*Appendix 1-16*).
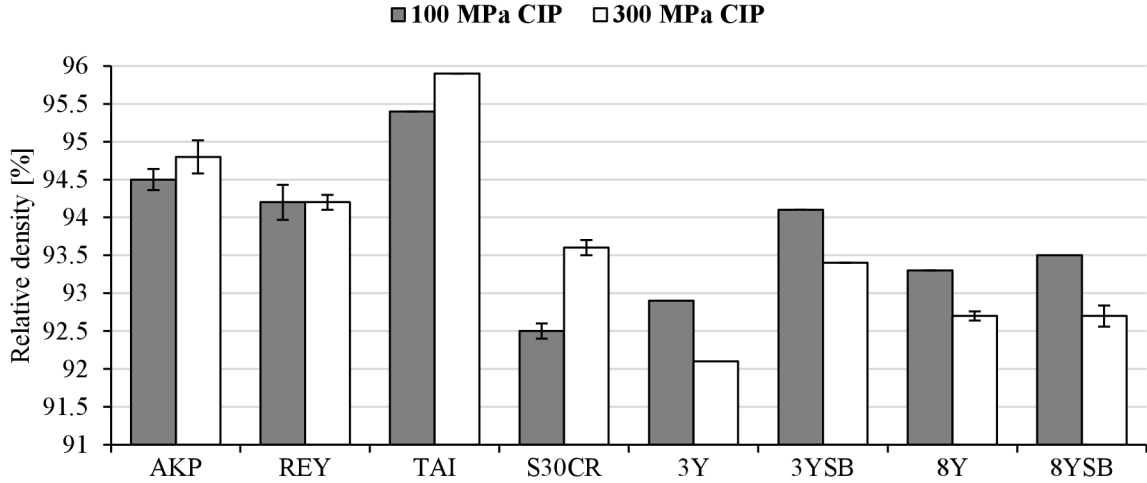
Figure 38: Summary of evaluated relative density when open porosity closes.

Table 2: Summarized values of nearly critical relative densities and corresponding values of open and closed porosity for used materials.

Material	Powder	CIP pressure [MPa]	ρ_{rel} [%]	s ρ_{rel} [-]	Vo [%]	s Vo [-]	Vc [%]	s Vc [-]
Alumina	AKP	100	94.5	0.09	0.1	0.4	5.3	0.17
		300	94.2	0.22	0.1	0.22	5.7	0.06
	REY	100	94.2	0.1	0.1	0.23	5.7	0.14
		300	94.2	0.1	0.1	0.10	5.8	0.04
	TAI	100	95.4	0.1	0.0	0.00	4.6	0.06
		300	95.9	0.1	0.0	0.00	4.1	0.05
Spinel	S30CR	100	92.5	0.34	0.0	0.1	7.5	0.3
		300	93.6	0.16	0.1	0.1	6.3	0.2
Tetragonal zirconia	3Y	100	92.9	0.15	0.0	0.00	7.1	0.15
		300	92.1	0.02	0.0	0.00	7.9	0.02
	3YSB	100	94.1	0.1	0.0	0.00	5.9	0.13
		300	93.4	0.1	0.1	0.06	6.5	0.01
Cubic zirconia	8Y	100	93.3	0.03	0.0	0.06	6.7	0.08
		300	92.7	0.2	0.1	0.14	7.2	0.06
	8YSB	100	93.5	0.16	0.0	0.15	6.4	0.31
		300	92.7	0.2	0.1	0.12	7.2	0.20

ρ_{rel} is relative density, Vo is volume of open porosity, Vc is volume of closed porosity, s is standard deviation calculated from 3 measurements

4.5 Reproducibility of Results

Reproducibility of the measurements was tested using samples with different size and different position in CIPed discs (*Figure 39*) sintered at different temperature. Results of these experiments are visible in *Figure 40* and in *Table 3*. The 1st sample is 1/4 of disc (including microstructure centre-middle-edge), the 2nd sample is cut from edge, the 3rd is cut from middle and the 4th sample is cut from centre of the disc.

This partial experiment shows, that CIP produces quite homogeneous green bodies with deviation only about ±0.13% t.d. after sintering. The second part of this experiment is to determine, whether size of sample plays role in relative density measurements. The results show that the relative density of samples with different size, but sintered at the same temperature differs about ±0.15% t.d.
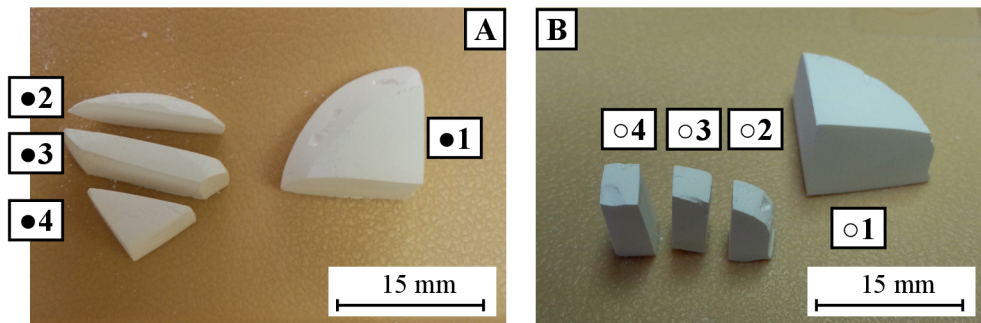
Figure 39: Disc cut into 4 pieces. A) are sintered at 1340 °C and B) are sintered at 1355 °C.
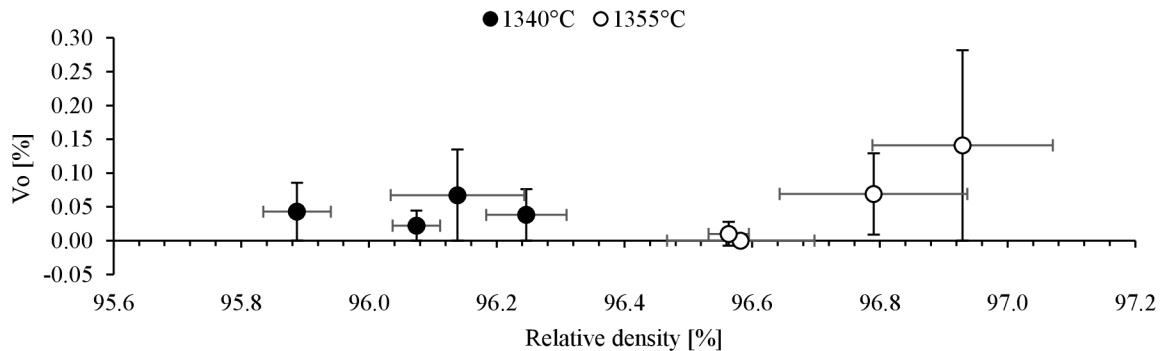
Figure 40: Results of reproducibility experiments.

Table 3: Relative densities and open porosity volumes for ● and ○ samples.

Sample	Temp. [°C]	ρ_{rel} [%]	s ρ_{rel} [-]	Vo [%]	s Vo [-]
●1	1340	96.2	0.1	0.0	0.01
●2	1340	96.1	0.1	0.1	0.12
●3	1340	96.1	0.0	0.0	0.02
●4	1340	95.9	0.1	0.0	0.00
○1	1355	96.6	0.0	0.0	0.02
○2	1355	96.6	0.1	0.0	0.00
○3	1355	96.9	0.1	0.1	0.14
○4	1355	96.8	0.1	0.1	0.06

ρ_{rel} is relative density, Vo is volume of open porosity,
s is standard deviation calculated from 3 measurements

5 DISCUSSION

5.1 Attempts of Critical Density Determination

In the literature, there are only few attempts to analyse pore evolution, all of them were focused on UO_2. The motivation for interlinked porosity research was deeply associated with fuel containment damage. When ceramic fuel (UO_2) undergoes nuclear fission, neutrons create more and more vacancies in bulk capsule and cause phenomena, which can be called "pore opening". Newly formed open porosity tunnels provide a direct route for the release of fission gas from interior regions of fuel, that causes damage to containment [51]. Comparison experimental data with theoretical models of instability of open porosity is very promising. Observations from these experiments [52, 53] and theoretical approaches [40, 51] show that UO_2 closes pores at 95% of theoretical density.

In this master's thesis several materials (alumina, tetragonal zirconia, cubic zirconia and magnesium spinel) with various lattices (hexagonal, tetragonal and cubic) and various particle size were used to determine critical relative density of the pore transformation in larger scale and in more general manner. There was also ambition to use theoretical models to support experimental data. To efficiently discuss this complex problem, it would be appropriate to divide this chapter into several sub-chapters devoted to each material.

5.2 Theoretical Calculations of Critical Density

Two theoretical models (Beere's - chapter 2.4.4 and Carter's & Gleaser's - chapter 2.4.5) were used to evaluate critical density for used materials. Models are based on uniform periodical tetrakaidecahedron structures, therefore transformation from open to close porosity occurs at once, because grains are same size and thus critical edge-length is the same for all tubular pores on grain edges. This, of course, do not happen under real conditions, where powder particles have some sort of distribution, grains are not of the same size, which produce variations in length of grain edges. Variations in microstructure in real sintered material could cause deviation of values calculated theoretically from values measured experimentally.

5.2.1 Dihedral Angle Values

To define critical porosity values from theoretical models, dihedral angles for used materials and for sintering temperatures have to be acquired. The dihedral angle can be calculated using Eq. 4 and known interfacial energies. Values of grain boundary interfacial energies and solid-vapour interfacial energies were obtained from available literature [54-56]. These articles provide temperature dependence of interfacial energies. Unfortunately, values of interfacial energies for tetragonal zirconia have not been found. Interfacial energies and calculated dihedral angles are summarized in *Table 4*:

Table 4: Summary of interfacial energies and calculated dihedral angle for used materials

Material	γ_{ss} [J·m^{-2}]	γ_{sv} [J·m^{-2}]
Al_2O_3 [54]	$1.913 - 0.611 \times 10^{-3} \cdot T$	$2.559 - 0.784 \times 10^{-3} \cdot T$
ZrO_2 (8% Y_2O_3) [55]	$1.215 - 0.358 \times 10^{-3} \cdot T$	$1.927 - 0.428 \times 10^{-3} \cdot T$
$MgAl_2O_4$ [56]	$2.340 - 0.451 \times 10^{-3} \cdot T$	$3.000 - 0.577 \times 10^{-3} \cdot T$

γ_{ss}-interfacial solid-solid energy, γ_{sv}-interfacial solid-vapour energy, T-temperature in K, ψ-dehedral angle

As it was mentioned above, interfacial energies, thus calculated dihedral angles vary with temperature. However, it is clearly visible from *Table 5*, that in the range of sintering temperatures 1300 °C - 1600 °C (see *Appendix 1-16*) dihedral angle could be taken as constant value for given material.

Table 5: Dihedral angle change with temperature for used materials

Temperature [°C]	Al_2O_3 [deg.]	ZrO_2 (8% Y_2O_3) [deg.]	$MgAl_2O_4$ [deg.]
1300	159.32	165.06	157.53
1400	159.43	165.39	157.53
1500	159.56	165.73	157.54
1600	159.70	166.11	157.54

5.2.2 Results of Calculations of Critical Porosity by Theoretical Models

Dihedral angle values were used to determine critical porosity from Beere's (*Figure 41*) and Carter & Gleaser's (*Figure 42*) models. Critical porosity differs from material to material in correlation with dihedral angle change. With increasing dihedral angle also critical porosity increases, which means that material will close open pores at a lower relative density.
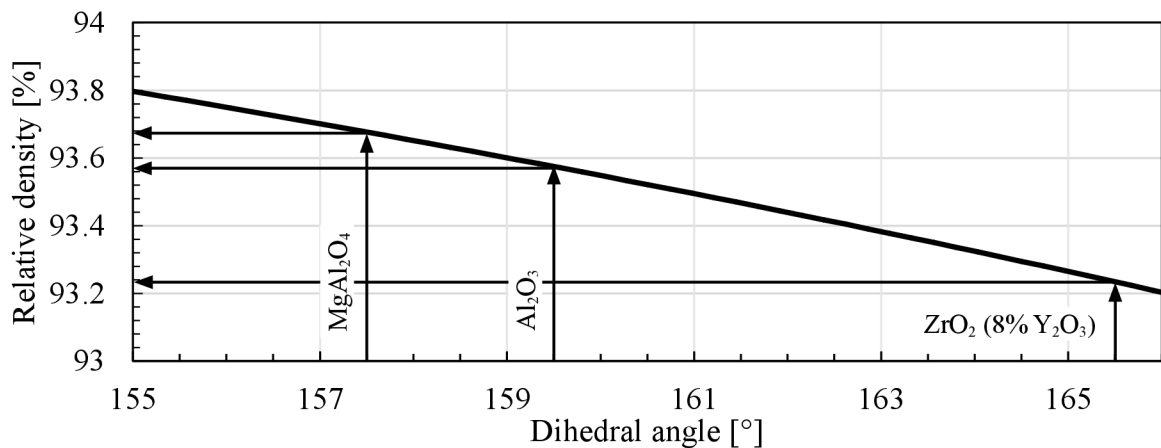
Figure 41: Critical porosity determination in Beere's model.
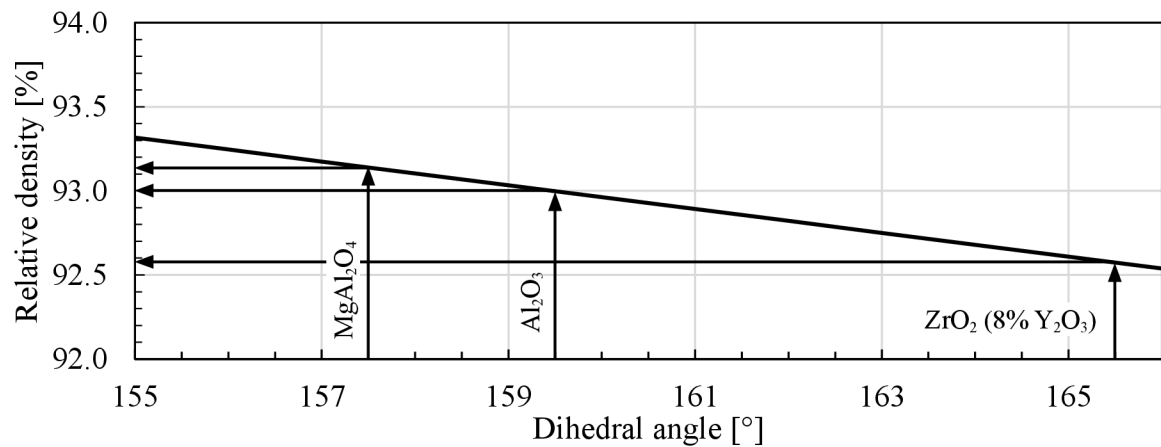
Figure 42: Critical porosity determination in C&G's model.

Table 6 shows calculated critical porosity based on dihedral angle of the used materials according to two used models. However, results show only minor difference in terms of values of relative densities, which is the consequence of similar dihedral angles.

Table 6: Dihedral angle and calculated critical relative density

Material	ψ (for 1300 - 1600 °C)	Beere's model	C&G's model
Al_2O_3	159.5°	93.6% t.d.	93.0% t.d.
ZrO_2 (3% Y_2O_3)	-	-	-
ZrO_2 (8% Y_2O_3)	165.5°	93.2% t.d.	92.6% t.d.
$MgAl_2O_4$	157.5°	93.7% t.d.	93.1% t.d.

5.3 Analyse of Critical Density for Alumina

Calculations from two theoretical models show critical porosity for Al_2O_3 at 93 and 93.6% of theoretical density. Several articles [9-17] about manufacturing transparent alumina ceramics by post-HIP procedure show that samples suitable for HIP have to be sintered above 95-96% of theoretical density to guarantee closed porosity. Experimental measurements of this master's thesis show very similar results: 95-96% of theoretical density as it is shown in *Table 7*. Validity of these results can be supported by paper focusing on grain growth in alumina ceramics [57]. According to the work, extensive grain growth starts at 97-98% t.d., which usually occurs after the open porosity transforms.

Table 7: Critical relative density comparison for alumina material.

Master's Thesis	Literature	Beere's model	C&G's model
95-96% t.d.	95-96% t.d.	93.6% t.d.	93.0% t.d.

The difference between experimental values and values from theoretical models can be explained by lattice symmetry of alumina crystals. Alumina has hexagonal lattice (*Figure 43*), which provides anisotropy in respect of energetic values of crystallographic planes. This anisotropy may extend the open porosity stage, via preventing microstructure to coarse (grain growth).
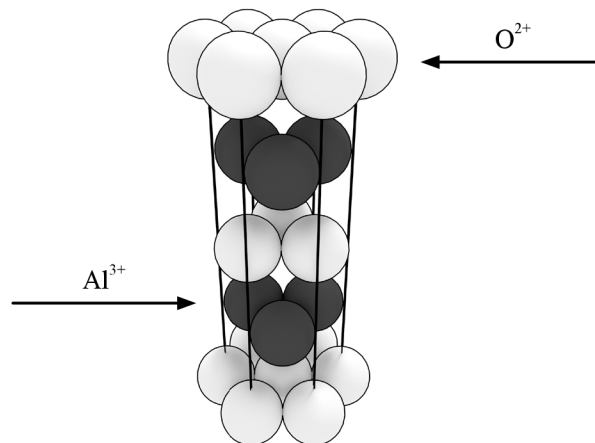
Figure 43: Hexagonal lattice of alumina material.

In the polycrystalline ceramic materials neighbouring grains are randomly oriented and create grain boundaries. To meet basic requirement of sintering (lowering energy of the system) grain boundaries have to be minimized, which is provided via grain boundary motion and via rotating and aligning crystallographic planes (*Figure 44*). After the grains rotate into crystal alignment the grain boundaries are eliminated [25].

Grain boundaries

A — Misaligned crystal planes

B — Aligned crystal planes

C — Grain coalescence (growth)
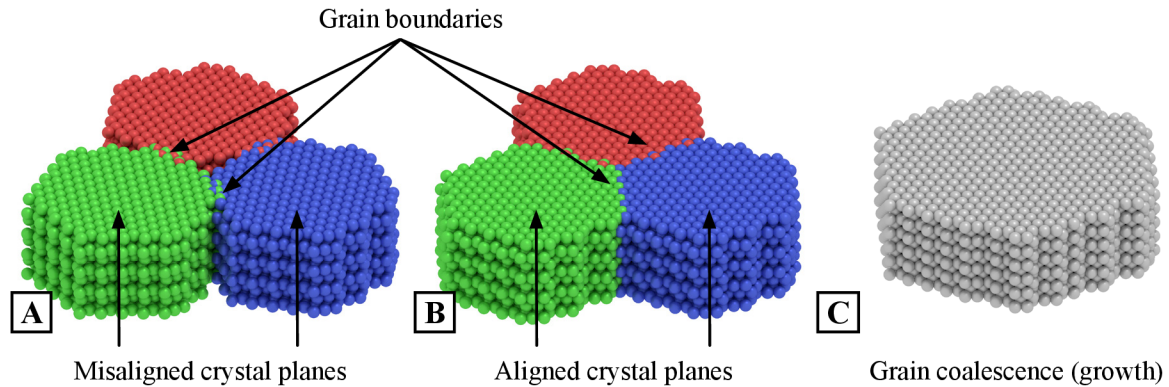
Figure 44: A schematic of grain coalescence during sintering. Three grains come into contact during sintering with random orientation of crystal planes (differentiated by colour) which turns into grain boundaries (A). To remove grain boundaries and lower the surface energy crystal planes have to rotate and align (B). Final step is fusing of grains to single grain (C).

Alumina with hexagonal lattice have higher probability to create large misorientation at grain boundaries due to lower lattice symmetry and therefore more energy is required to align crystallographic planes to start grain growth and to reach Rayleigh criterion for pore closure (Chapter 2.4.2).

Another explanation of deflection from values from theoretical models is questioning the interfacial energies acquired from literature [54]. In this thesis all alumina powders are doped by 250 ppm of MgO (to prevent exaggerated grain growth) which segregates on grain boundaries and decreases their mobility [57]. However, used material for determination of interfacial energies in paper [54] was not probably doped, because it is powder used mainly for processes of casting metals and therefore there are not high demands for idealised microstructure of ceramics. MgO segregated on grain boundaries could change values of interfacial energies and thus dihedral angle. To prove this theory, interfacial energies for used powders (AKP, REY, TAI) will be tested by sessile drop method in near future.

As another explanation of deviation from theoretical models, homogeneity of microstructure could be suggested. Structure analysis will be made to prove or disconfirm this hypothesis.

5.4 Analyse of Critical Density for Zirconia

Calculations according to Beere's and C&G's model show critical porosity for cubic (8mol% Y_2O_3) ZrO_2 at 93.2 and 92.6% of theoretical density, respectively. Unfortunately, data of interfacial energies for tetragonal (3mol% Y_2O_3) ZrO_2 have not been found, thus neither dihedral angle nor critical relative density is available for this material.

One article dealing with cubic zirconia [18] and several [19-22] papers dealing with tetragonal zirconia focused on manufacturing zirconia ceramics by post-HIP procedure provide values of critical relative densities. These articles show that samples suitable for HIP have to be sintered above 94% of theoretical density to guarantee closed porosity for tetragonal zirconia

and above 92% of theoretical density for cubic zirconia. Experimental measurements of this master's thesis show only slightly different results: around 93 - 93.5% of theoretical density for cubic zirconia and 92 - 94% for tetragonal zirconia as shown in *Table 8*.

Table 8: Critical relative density comparison for zirconia material.

Zirconia	Master's Thesis	Literature	Beere's model	C&G's model
Tetragonal	92-94% t.d.	94% t.d.	-	-
Cubic	93-93.5% t.d.	92% t.d.	93.2% t.d.	92.6% t.d.

Scatter in relative density values of zirconia from master's thesis, although it is very small, originates from different cold isostatic pressure during shaping process. Differences in relative density of 100 MPa and 300 MPa samples could be explained by influence of pore coordination number. As our experimental results show (*Figure 38*), low pressed samples tend to close pores at higher relative densities.

Lower CIP pressure cause lower initial density of green body and increased existence of large pores with high coordination number (many particles surrounding the pore) and therefore high energy is required to remove such pores. Higher sintering temperature is needed to change radius of curvature inside pore via removing grain boundaries during grain coalescence. According to [58] coordination number directly influences pore closure (*Figure 45*).
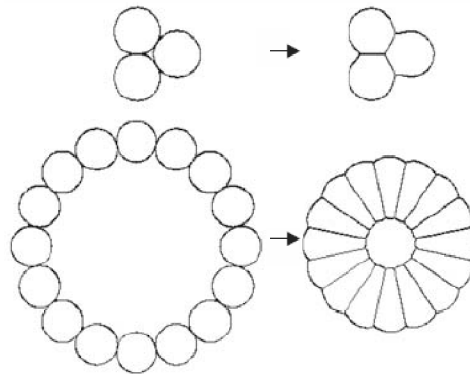
Figure 45: Transformation of regular pore packing: Upper illustrates coordination number 3 and lower illustrates coordination number 16 [58].

As one can see there is sufficient agreement between experimental data of cubic zirconia and theoretical calculations. In this situation, the same explanation like with alumina material can be used: cubic lattice is highly symmetrical and therefore necks in the first stage of sintering is formed easily and in high numbers, which provides faster sintering and densification. Same situation happens in the second stage of sintering, where grain boundaries are eliminated easier because of higher probability for achieving grain boundary confirmation, which will lead to grain growth and alternatively to closure of interconnected pores. Rayleigh criterion (Chapter 2.4.2) is met at lower density.

5.5 Analyse of Critical Density for Spinel

Calculations from the theoretical models show critical density for $MgAl_2O_4$ 93.7% t.d. (Beere's model) and 93.1% t.d. (C&G's model). Data found in literature [50] show, that relative density of samples suitable for HIP treatment have to be around 94% t.d. Experimental

measurements performed in this master's thesis show very similar results: 93.6% t.d. for 300 MPa CIPed samples. However, samples CIPed 100 MPa show relative big difference (92.5% t.d.) as it is visible from *Table 9*.

Table 9: Critical relative density comparison for spinel material.

Master's Thesis	Literature	Beere's model	C&G's model
93.6% t.d. (92.5% t.d.)	94% t.d.	93.7% t.d.	93.1% t.d.

Difference cannot be explained by coordination number theory as it was discussed above for zirconia, because the drop in critical relative density occurs in opposite manner - samples CIPed by higher pressure closes sooner than samples CIPed by lower pressure. Explanation of this phenomena could be the goal of next study.

Spinel has, in spite of its complexity cubic crystallographic lattice. Due this fact, there is very similar situation like with cubic zirconia. Both these materials have cubic lattice and in both cases experimental measurements correspond (very successfully) with theoretical models.

5.6 Comparison of Critical Density for Used Materials

Figure 46 shows comparison among experimental data acquired in this master's thesis, from the literature and from the theoretical models. To be able to compare all data, the experimental results of this thesis, as well as experimental results from literature are present as a average value for given material regardless of initial particle size and shaping methods.
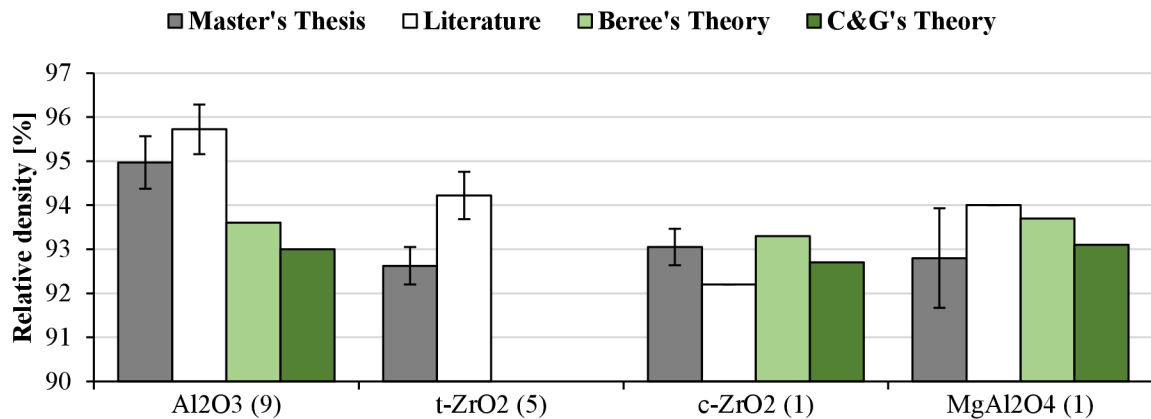
Figure 46: Summarized comparison of critical density of all available data. Numbers next to labels represent amount of articles with critical density information.

Theoretical models exhibit that critical density is only material characteristic depending only on interfacial energies, thus on dihedral angle, independently on particle size and used shaping technique. For cubic systems (cubic zirconia and spinel) one can see that experimental values either from this thesis or from experiments in literature agreed only with minor differences. Comparison for tetragonal system (tetragonal zirconia) can be made only with literature experimental data and in this case, critical density in literature is slightly higher.

However, results of critical density for alumina from this thesis and from literature exhibit different values that from theoretical models. This issue is discussed in chapter 5.3 and will be the subject of subsequent research.

6 CONCLUSIONS

According to author's knowledge, in this master's thesis it has been performed the most extensive research of critical density (i.e. the density when tubular open pores turn to isolated closed pores). It has been analysed using two theoretical models how dihedral angle in various ceramic materials influences the critical density. These values were confronted with the experimental values obtained in this work and with experimental values used in post-HIP treatments acquired from the literature.

This research is extremely important, e.g. for producing of transparent armours and missile domes, dense bone and joint implants, cutting tools etc. Up to now the conditions for post-HIP treatment were determined mostly from expensive and time consuming trial-and-error experiments, therefore the deep research in this field is highly desirable.

Experimental part of this master's thesis has been focused on evaluation of critical density of various materials (alumina, tetragonal and cubic zirconia, alumina-magnesia spinel), with different particle size and with different microstructure of green body. With consideration of all gathered data, following comparison can be made:

- Al_2O_3
  Our experimental results show good agreement with other literature experimental data in term of critical density (95-96% t.d.). However, theoretical calculations show a bit lower critical density (93-93.7% t.d.). Several hypotheses explaining this difference as well as future approaches to explain these phenomena were suggested.
- Cubic ZrO_2
  Our results show good agreement of critical density (92-93% t.d.) with data from the literature and also with theoretical calculations.
- Tetragonal ZrO_2
  Our results of critical density (92-94% t.d.) were in agreement with literature results (94% t.d.). Unfortunately, the thermodynamic data for calculations of theoretical critical density of this material are not available, therefore the further effort will be devoted to obtain the values of interfacial energies by the sessile drop method.
- $MgAl_2O_4$
  Our results show good agreement of critical density in case of 300 MPa CIPed samples (93.6% t.d.) with data from literature (94% t.d.) and also with data from theoretical models (93.1-93.7% t.d.). However, samples CIPed at 100 MPa show yet unexplained behaviour and close pores at 92.5% t.d.

Used theoretical models utilised in this work are based on thermodynamic laws. Low heating rate (5 °C/min) used it this work can be considered as near-equilibrium approximation, therefore results of theoretical calculations could be successfully compared with results of sintering experiments of this thesis. In the future, it could be also very interesting to use so called fast sintering (heating rate 100-200 °C/min) and study behaviour of the system out of the thermodynamic equilibrium.

7 REFERENCES

[1] BASU, Bikramjit and Kantesh BALANI. *Advanced structural ceramics*. Hoboken, N.J.: Wiley, 2011, xxvi, 474 p.

[2] PARK, Joon Bu and Roderic S LAKES. *Biomaterials: an introduction*. 3rd ed. New York: Springer, 2007, xi, 561 p. ISBN 9780387378800-.

[3] TRUNEC, Martin and Karel MACA. *Advanced Ceramic Processes. Advanced Ceramics for Dentistry*. Elsevier, 2014, s. 123. DOI: 10.1016/B978-0-12-394619-5.00007-9.

[4] NAIR, K and Shashank PRIYA. *Advances and applications in electroceramics II*. Westerville, Ohio: American Ceramic Society, 2012, xi, 244 p.

[5] WANG, S.F., J. ZHANG, D.W. LUO, F. GU, D.Y. TANG, Z.L. DONG, G.E.B. TAN, W.X. QUE, T.S. ZHANG, S. LI and L.B. KONG. Transparent ceramics: Processing, materials and applications. *Progress in Solid State Chemistry*. 2013, vol. 41, 1-2, s. 20-54 DOI: 10.1016/j.progsolidstchem.2012.12.002.

[6] RAHAMAN, M. *Ceramic processing and sintering*. 2nd ed. New York: M. Dekker, 2003, xiii, 875 p. Materials engineering (Marcel Dekker, Inc.), 23. ISBN 0824709888-.

[7] KANG, Suk-Joong L. *Sintering: densification, grain growth, and microstructure*. 1st ed. Burlington: Elsevier Butterworth-Heinemann, 2005, xii, 265 s. ISBN 0-7506-6385-5.

[8] GERMAN, Randall. *Sintering: from empirical observations to scientific principles*. First edition. Burlington: Elsevier Science, 2014. ISBN 978-012-4016-774.

[9] KRELL, Andreas, Jens KLIMKE a Thomas HUTZLER. Advanced spinel and sub-μm Al2O3 for transparent armour applications. *Journal of the European Ceramic Society*. 2009, vol. 29, issue 2, s. 275-281. DOI: 10.1016/j.jeurceramsoc.2008.03.024.

[10] APETZ, Rolf and BRUGGEN, Michel PB. Transparent Alumina: A Light-Scattering Model. *Journal of the American Ceramic Society*, 2003, 86.3: 480-486.

[11] PETIT, Johan, Philippe DETHARE, Alessandra SERGENT, Robert MARINO, Marie-Hélène RITTI, Stéphane LANDAIS, Jean-Luc LUNEL and Sandrine TROMBERT. Sintering of α-alumina for highly transparent ceramic applications. *Journal of the European Ceramic Society*. 2011, vol. 31, issue 11, s. 1957-1963. DOI: 10.1016/j. jeurceramsoc.2011.04.034.

[12] KRELL, Andreas, Paul BLANK, Hongwei MA, Thomas HUTZLER, Michel P. B. BRUGGEN and Rolf APETZ. Transparent Sintered Corundum with High Hardness and Strength. *Journal of the American Ceramic Society*. 2003, vol. 86, issue 1, s. 12-18. DOI: 10.1111/j.1151-2916.2003.tb03270.x.

[13] NISHIYAMA, Norimasa, Takashi TANIGUCHI, Hiroaki OHFUJI, Kimiko YOSHIDA, Fumihiro WAKAI, Byung-Nam KIM, Hidehiro YOSHIDA, Yuji HIGO, Astrid HOLZHEID, Oliver BEERMANN, Tetsuo IRIFUNE, Yoshio SAKKA and Ken-ichi FUNAKOSHI. Transparent nanocrystalline bulk alumina obtained at 7.7 GPa and 800 °C. *Scripta Materialia*. 2013, vol. 69, issue 5, s. 362-365. DOI: 10.1016/j. scriptamat.2013.05.017.

[14] TRUNEC, Martin, Karel MACA and Radim CHMELIK. Polycrystalline alumina ceramics doped with nanoparticles for increased transparency. *Journal of the European Ceramic Society*. 2015, vol. 35, issue 3, s. 1001-1009. DOI: 10.1016/j.jeurceramsoc.2014.09.041.

[15] MA, J. and L.C. LIM. Effect of particle size distribution on sintering of agglomerate-free submicron alumina powder compacts. *Journal of the European Ceramic Society*. 2002, vol. 22, issue 13, s. 2197-2208. DOI: 10.1016/s0955-2219(02)00009-2.

[16] SHINOHARA, Nobuhiro, Masataro OKUMIYA, Tadashi HOTTA, Kenji NAKAHIRA,

Makio NAITO and Keizo UEMATSU. Morphological Changes in Process-Related Large Pores of Granular Compacted and Sintered Alumina. *Journal of the American Ceramic Society*. 2000, vol. 83, issue 7, s. 1633-1640. DOI: 10.1111/j.1151-2916.2000.tb01442.x.

[17] NETTLESHIP, Ian, Richard J. MCAFEE and William S. SLAUGHTER. Evolution of the Grain Size Distribution during the Sintering of Alumina at 1350 °C. *Journal of the American Ceramic Society*. 2002, vol. 85, issue 8, s. 1954-1960. DOI: 10.1111/j.1151-2916.2002.tb00387.x.

[18] LACH, Radosław, Mirosław M. BUĆKO, Krzysztof HABERKO, Maciej SITARZ and Katarzyna CHOLEWA-KOWALSKA. From nanometric zirconia powder to transparent polycrystal. *Journal of the European Ceramic Society*. 2014, vol. 34, issue 16, s. 4321-4326. DOI: 10.1016/j.jeurceramsoc.2014.07.004.

[19] KLIMKE, Jens, Martin TRUNEC and Andreas KRELL. Transparent Tetragonal Yttria-Stabilized Zirconia Ceramics: Influence of Scattering Caused by Birefringence. *Journal of the American Ceramic Society*. 2011, vol. 94, issue 6, s. 1850-1858. DOI: 10.1111/j.1551-2916.2010.04322.x.

[20] MAZAHERI, Mehdi, A. SIMCHI and F. GOLESTANI-FARD. Densification and grain growth of nanocrystalline 3Y-TZP during two-step sintering. *Journal of the European Ceramic Society*. 2008, vol. 28, issue 15, s. 2933-2939. DOI: 10.1016/j.jeurceramsoc.2008.04.030.

[21] TRUNEC, Martin and Karel MACA. Processing and Properties of Nanocrystalline Tetragonal Zirconia. *Key Engineering Materials*. 2007, 336-338, s. 2300-2303. DOI: 10.4028/www.scientific.net/kem.336-338.2300.

[22] KIM, Jin-Young, Nozomu UCHIDA, Katsuichi SAITO and Keizo UEMATSU. Analysis of Hot Isotatic Pressing of Presintered Zirconia. *Journal of the American Ceramic Society*. 1990, vol. 73, issue 4, s. 1069-1073. DOI: 10.1111/j.1151-2916.1990.tb05158.x.

[23] MAYO, M. J. Processing of nanocrystalline ceramics from ultrafine particles. *International Materials Reviews*. 1996-01-01, vol. 41, issue 3, s. 85-115. DOI: 10.1179/095066096790326039.

[24] KINGERY, W. *Ceramic fabrication processes*. Cambridge: Technology Press of Massachusetts Institute of Technology, 1958, xi, 235 p.

[25] GERMAN, Randall. *Sintering: from empirical observations to scientific principles*. First edition. Burlington: Elsevier Science, 2014. ISBN 978-012-4016-774.

[26] COBLE, R. L. Sintering Crystalline Solids. I. Intermediate and Final State Diffusion Models. *Journal of Applied Physics*. 1961, vol. 32, issue 5. DOI: 10.1063/1.1736107.

[27] KRELL, Andreas and Paul BLANK. Grain Size Dependence of Hardness in Dense Submicrometer Alumina. *Journal of the American Ceramic Society*. 1995, vol. 78, issue 4, s. 1118-1120. DOI: 10.1111/j.1151-2916.1995.tb08452.x.

[28] KRELL, Andreas and Paul BLANK. The Influence of shaping method on the grain size dependence of strength in dense submicrometre alumina. *Journal of the European Ceramic Society*. 1996, vol. 16, issue 11, s. 1189-1200. DOI: 10.1016/0955-2219(96)00044-1.

[29] KRELL, Andreas and Dieter KLAFFKE. Effects of Grain Size and Humidity on Fretting Wear in Fine-Grained Alumina, Al2O3/TiC, and Zirconia. *Journal of the American Ceramic Society*. 1996, vol. 79, issue 5, s. 1139-1146. DOI: 10.1111/j.1151-2916.1996.tb08565.x.

[30] HE, Yingjie, Louis WINNUBST, Anthonie J. BURGGRAAF, Henk VERWEIJ, Paul G. Th. VARST and Bert WITH. Grain-Size Dependence of Sliding Wear in Tetragonal Zirconia Polycrystals. *Journal of the American Ceramic Society*. 1996, vol. 79, issue 12, s. 3090-3096. DOI: 10.1111/j.1151-2916.1996.tb08081.x.

[31] LAWSON, Simon. Environmental degradation of zirconia ceramics. *Journal of the European Ceramic Society*. 1995, vol. 15, issue 6, s. 485-502. DOI: 10.1016/0955-2219(95)00035-s.

[32] XU, G. Grain Size-dependent Electrical Conductivity in Ccandia-stabilized zirconia Prepared by a Mild Urea-based Hydrothermal Method. *Solid State Ionics*. 2004, vol. 166, 3-4, s. 391-396. DOI: 10.1016/j.ssi.2003.11.014.

[33] KLIMKE, Jens, Martin TRUNEC and Andreas KRELL. Transparent Tetragonal Yttria-Stabilized Zirconia Ceramics: Influence of Scattering Caused by Birefringence. *Journal of the American Ceramic Society*. 2011, vol. 94, issue 6, s. 1850-1858. DOI: 10.1111/j.1551-2916.2010.04322.x.

[34] APETZ, Rolf and Michel P. B. BRUGGEN. Transparent Alumina: A Light-Scattering Model. *Journal of the American Ceramic Society*. 2003, vol. 86, issue 3, s. 480-486. DOI: 10.1111/j.1151-2916.2003.tb03325.x.

[35] KUCZYNSKI, G. C. Self-Diffusion in sintering of merallic particles. *AIME Metals Transactions*. 1949, Vol. 185, s. 169-178. DOI: 10.1007/978-94-009-0741-6_33

[36] BUDWORTH, W.D. Theory of Pore Closure during Sintering. *Transactions of the British Ceramic Society*. 1970, č. 69, s. 29-31.

[37] RAYLEIGH, L. On The Instability Of Jets. *Proceedings of the London Mathematical Society*. 1878, s1-10, issue 1, s. 4-13. DOI: 10.1112/plms/s1-10.1.4.

[38] GUPTA, T. K. Instability of Cylindrical Voids in Alumina. *Journal of the American Ceramic Society*. 1978, vol. 61, 5-6, s. 191-195. DOI: 10.1111/j.1151-2916.1978.tb09276.x.

[39] NICHOLS, F. A. and W. W. MULLINS. Morphological Changes of a Surface of Revolution due to Capillarity-Induced Surface Diffusion. *Journal of Applied Physics*. 1965, vol. 36, issue 6. DOI: 10.1063/1.1714360.

[40] BEERE, W. A unifying theory of the stability of penetrating liquid phases and sintering pores. *Acta Metallurgica*. 1975, vol. 23, issue 1, s. 131-138. DOI: 10.1016/0001-6160(75)90078-4.

[41] CARTER, W.C., A.M. GLAESER, W. Craig CARTER and Andreas M. GLAESER. The morphological stability of continuous intergranular phases: Thermodynamic considerations. *Acta Metallurgica*. 1987, vol. 35, issue 1, s. 15-26. DOI: 10.1007/978-1-4613-2233-7_2.

[42] KINGERY, W. D. and B. FRANCIS. Grain Growth in Porous Compacts. *Journal of the American Ceramic Society*. 1965, vol. 48, issue 10, s. 546-547. DOI: 10.1111/j.1151-2916.1965.tb14665.x.

[43] SŌMIYA, Shigeyuki and Yūsuke MORIYOSHI. *Sintering Key Papers*. New York: Elsevier Applied Science, 1990, xi, 801 p. ISBN 1851663223.

[44] KWON, Sung-Tae, Doh-Yeon KIM, Thae-Khapp KANG and Duk N. YOON. Effect of Sintering Temperature on the Densification of Al2O3. *Journal of the American Ceramic Society*. 1987, vol. 70, issue 4, C-69-C-70. DOI: 10.1111/j.1151-2916.1987.tb04987.x.

[45] RIEDEL, R. *Ceramics science and technology*. Weinheim: Wiley-VCH, 2008, xxii, 590 s. ISBN 978-3-527-31155-2.

[46] WANG, S.F., J. ZHANG, D.W. LUO, F. GU, D.Y. TANG, Z.L. DONG, G.E.B. TAN, W.X. QUE, T.S. ZHANG, S. LI and L.B. KONG. Transparent Ceramics: Processing, Materials and Applications. *Progress in Solid State Chemistry*. 2013, vol. 41, 1-2, s. 20-54. DOI: 10.1016/j.progsolidstchem.2012.12.002.

[47] TRUNEC, Martin, Karel MACA and Radim CHMELIK. Polycrystalline Alumina Ceramics Doped with Nanoparticles for Increased Transparency. *Journal of the European Ceramic*

Society. 2015, vol. 35, issue 3, s. 1001-1009. DOI: 10.1016/j.jeurceramsoc.2014.09.041.

[48] PEUCHERT, Ulrich, Yoshio OKANO, Yvonne MENKE, Steffen REICHEL and Akio IKESUE. Transparent Cubic-ZrO2 Ceramics for Application as Optical Lenses. *Journal of the European Ceramic Society*. 2009, vol. 29, issue 2, s. 283-291. DOI: 10.1016/j.jeurceramsoc.2008.03.028.

[49] CHAIM, R. and M. HEFETZ. Fabrication of Dense Nanocrystalline ZrO2−3 wt. % Y2O3 by Hot-isostatic Pressing. *Journal of Materials Research*. 1998, vol. 13, issue 07, s. 1875-1880. DOI: 10.1557/jmr.1998.0266.

[50] MACA, Karel, Martin TRUNEC and Radim CHMELIK. Processing and Properties of Fine Grained Transparent MgAl2O4 Ceramics. *Ceram.-Silik*. 2007, č. 51, s. 94-97.

[51] TUCKER, M. O. and J. A. TURNBULL. The Morphology of Interlinked Porosity in Nuclear Fuels. *Proceedings of the Royal Society A: Mathematical, Physical and Engineering Sciences*. 1975, vol. 343, issue 1634, s. 299-314. DOI: 10.1098/rspa.1975.0067.

[52] THUMMLER, F. and W. THOMMA. The sintering process. Met. Rev. 1967, č. 12, s.69-108

[53] COLEMAN, S. C. and W. B. BEERÉ. The Sintering of Open and Closed Porosity in UO2. *Philosophical Magazine*. 1975, vol. 31, issue 6, s. 1403-1413. DOI: 10.1080/00318087508228691.

[54] NIKOLOPOULOS, P. Surface, Grain-boundary and Interfacial Energies in Al2O3 and Al2O3-Sn, Al2O3-Co Systems. *Journal of Materials Science*. 1985, vol. 20, issue 11, s. 3993-4000. DOI: 10.1007/bf00552390.

[55] TSOGA, A. and P. NIKOLOPOULOS. Surface and Grain-boundary Energies in Yttria-stabilized Zirconia (YSZ-8 mol%). *Journal of Materials Science*. 1996, vol. 31, issue 20, s. 5409-5413. DOI: 10.1007/bf01159310.

[56] BRUCE, R.H. 1965. Aspects of surface energy of ceramics. *Science of ceramics*. (2): 359-381.

[57] MACA, Karel, Václav POUCHLÝ, Katarína BODIŠOVÁ, Peter ŠVANČÁREK and Dušan GALUSEK. Densification of fine-grained alumina ceramics doped by magnesia, yttria and zirconia evaluated by two different sintering models. *Journal of the European Ceramic Society*. 2014, vol. 34, issue 16, s. 4363-4372. DOI: 10.1016/j.jeurceramsoc.2014.06.030.

[58] GALAKHOV, A. V. Pore coordination number and sintering. *Refractories and Industrial Ceramics*. 2010, vol. 51, issue 2, s. 83-87. DOI: 10.1007/s11148-010-9264-y.

8 APPENDIX

Appendix 1: Measured relative density, open and closed porosity for AKP 100 MPa CIP

Sample	Temperature [°C]	Relative density [%]	s [-]	V_O [%]	V_C [%]
Ax0	800	56.4	0.25	43.4	0.2
Ax1	1430	92.5	0.14	5.1	2.4
Ax7	1435	93.2	0.14	4.4	2.4
Ax6	1445	93.5	0.12	3.0	3.5
Ax4	1450	94.4	0.16	0.7	4.8
Ax5	1455	94.5	0.09	0.1	5.3
Ax52	1455	94.7	0.02	0.1	5.3
Ax42	1450	94.8	0.06	0.0	5.2
Ax43	1450	94.8	0.14	0.0	5.2
Ax54	1455	94.8	0.14	0.1	5.0
Ax53	1455	95.0	0.07	0.1	4.9
Ax23	1460	95.3	0.03	0.0	4.6
Ax22	1460	95.4	0.06	0.0	4.6
Ax2	1460	95.4	0.16	0.0	4.6

Vo is volume of open porosity, Vc is volume of closed porosity, s is standard deviation calculated from 3 measurements

Appendix 2: Measured relative density, open and closed porosity for AKP 300 MPa CIP

Sample	Temperature [°C]	Relative density [%]	s [-]	V_O [%]	V_C [%]
A0	800	58.2	0.57	41.4	0.4
A1	1400	89.5	0.49	9.1	1.4
A53	1415	92.1	0.02	5.8	2.1
A52	1415	92.3	0.08	5.5	2.2
A5	1415	93.0	0.18	4.5	2.5
A6	1420	93.6	0.03	3.0	3.5
A4	1425	93.8	0.29	1.5	4.8
A7	1430	94.1	0.18	1.5	4.4
A72	1430	94.2	0.22	0.1	5.7
A82	1435	94.7	0.18	0.1	5.2
A8	1435	94.8	0.16	0.0	5.2
A32	1440	95.1	0.05	0.0	4.9
A3	1440	95.3	0.15	0.0	4.7
A2	1450	95.4	0.20	0.4	4.2
A22	1450	96.2	0.20	0.0	3.8

Vo is volume of open porosity, Vc is volume of closed porosity, s is standard deviation calculated from 3 measurements

Appendix 3: Measured relative density, open and closed porosity for REY 100 MPa CIP

Sample	Temperature [°C]	Relative density [%]	s [-]	V_O [%]	V_C [%]
Bx0 - 800/60min	800	58.6	0.1	41.2	0.2
Bx3	1455	91.5	0.3	7.2	1.3
Bx2	1460	92.7	0.1	5.1	2.2
Bx8	1470	92.7	0.2	2.7	4.5
Bx82	1470	92.9	0.2	2.3	4.9
Bx1	1465	93.3	0.2	2.9	3.8
Bx4	1475	93.9	0.1	1.3	4.8
Bx62	1480	94.2	0.1	0.1	5.8
Bx63	1480	94.1	0.0	0.1	5.8
Bx6	1480	94.5	0.1	0.6	4.9
Bx73	1485	94.5	0.1	0.1	5.4
Bx72	1485	94.5	0.1	0.1	5.4
Bx7	1485	94.7	0.1	0.0	5.3
Bx52	1490	94.8	0.1	0.0	5.1
Bx53	1490	94.9	0.0	-0.1	5.2
Bx5	1490	95.3	0.1	0.0	4.7

Vo is volume of open porosity, Vc is volume of closed porosity, s is standard deviation calculated from 3 measurements

Appendix 4: Measured relative density, open and closed porosity for REY 300 MPa CIP

Sample	Temperature [°C]	Relative density [%]	s [-]	V_O [%]	V_C [%]
B0	800	59.7	0.2	39.6	0.7
B1	1400	85.2	0.4	14.3	0.5
B6	1425	89.5	0.2	10.0	0.5
B7	1460	92.1	0.0	6.1	1.8
B3	1450	92.5	0.2	5.4	2.1
B5	1455	92.9	0.1	4.4	2.6
B52	1455	93.1	0.1	1.5	5.4
B53	1455	93.1	0.3	1.6	5.3
B8	1460	93.5	0.1	3.0	3.5
B73	1460	93.9	0.1	0.7	5.5
B72	1460	93.9	0.1	0.2	5.9
B4	1465	93.9	0.3	0.7	5.5
B42	1465	94.2	0.1	0.1	5.8
B43	1465	94.2	0.2	0.1	5.7
B10	1470	94.3	0.1	0.0	5.7
B102	1470	94.4	0.0	0.1	5.5
B11	1475	94.9	0.1	0.1	5.0
B2	1480	95.1	0.2	0.2	4.8
B23	1480	95.4	0.2	0.1	4.5
B92	1485	95.4	0.1	0.0	4.6
B22	1480	95.5	0.3	0.0	4.5
B92	1485	95.7	0.1	0.0	4.3

Vo is volume of open porosity, Vc is volume of closed porosity, s is standard deviation calculated from 3 measurements

Appendix 5: Measured relative density, open and closed porosity for TAI 100 MPa CIP

Sample	Temperature [°C]	Relative density [%]	s [-]	V_O [%]	V_C [%]
Dx0	800	54.8	0.0	44.7	0.5
Dx1	1320	90.1	0.3	9.1	0.8
Dx2	1340	93.1	0.1	4.7	2.2
Dx3	1350	93.5	0.2	4.0	2.5
Dx23	1340	94.2	0.2	2.4	3.3
Dx22	1340	94.3	0.1	3.0	2.7
Dx63(33)	1350	94.1	0.4	2.8	3.2
Dx62(32)	1350	94.6	0.2	2.2	3.3
Dx32(62)	1345	94.8	0.1	0.9	4.3
Dx73	1355	94.8	0.0	2.1	3.1
Dx6	1345	94.9	0.1	0.1	5.0
Dx33(63)	1345	94.9	0.2	1.8	3.4
Dx72	1355	95.1	0.0	1.8	3.1
Dx5	1355	95.3	0.2	0.8	3.8
Dx7	1355	95.4	0.1	0.0	4.6
Dx4	1360	96.6	0.1	0.0	3.4

Vo is volume of open porosity, Vc is volume of closed porosity, s is standard deviation calculated from 3 measurements

Appendix 6: Measured relative density, open and closed porosity for TAI 300 MPa CIP

Sample	Temperature [°C]	Relative density [%]	s [-]	V_O [%]	V_C [%]
D0	800	56.6	0.3	43.0	0.4
D1	1320	91.6	0.4	7.1	1.3
D5	1327	93.2	0.1	4.3	2.5
D10	1325	94.3	0.2	1.4	4.3
D4	1335	94.4	0.1	1.1	4.4
D102	1325	94.6	0.1	1.0	4.4
D6	1340	94.8	0.1	0.8	4.4
D92	1345	96.1	0.3	0.0	3.9
D62	1340	96.3	0.0	0.1	3.6
D112	1330	96.5	0.0	0.0	3.4
D11	1330	96.6	0.1	0.1	3.4
D93	1345	96.8	0.1	0.0	3.1
D9	1345	96.9	0.2	0.0	3.1
D72 (42)	1355	96.9	0.1	0.0	3.1
D73 (43)	1355	96.9	0.0	0.0	3.1
D7	1355	97.1	0.2	0.0	2.9
D82	1350	97.2	0.1	0.0	2.8
D8	1350	97.2	0.2	0.0	2.8
D3	1360	97.4	0.1	0.0	2.6

Vo is volume of open porosity, Vc is volume of closed porosity, s is standard deviation calculated from 3 measurements

Appendix 7: Measured relative density, open and closed porosity for S30CR 100 MPa CIP

Sample	Temperature [°C]	Relative density [%]	s [-]	V_O [%]	V_C [%]
Cx1 - 1500/18min	1500	83.6	0.15	16.3	0.1
Cx2 - 1500/21min	1500	83.9	0.19	15.9	0.2
Cx3	1550	85.6	0.20	14.2	0.2
Cx5	1575	90.6	0.63	2.6	6.8
Cx52	1575	90.8	0.51	2.9	6.3
Cx62	1590	92.5	0.34	0.0	7.5
Cx6	1590	92.7	0.18	0.0	7.4
Cx4	1600	93.6	0.11	0.1	6.3
Cx42	1600	93.6	0.16	0.0	6.4

Vo is volume of open porosity, Vc is volume of closed porosity, s is standard deviation calculated from 3 measurements

Appendix 8: Measured relative density, open and closed porosity for S30CR 300 MPa CIP

Sample	Temperature [°C]	Relative density [%]	s [-]	V_O [%]	V_C [%]
C0	800	50.7	0.29	48.3	1.0
C1	1500	88.3	0.54	10.9	0.8
C4 - 1500/17min	1500	91.4	0.60	5.1	3.5
C122	1520	91.6	0.03	2.8	5.6
C122	1520	91.6	0.08	1.7	6.7
C3 - 1500/15min	1500	91.9	0.25	4.9	3.2
C2 - 1500/20min	1500	92.4	0.31	1.1	6.4
C6 - 1500/21min	1500	92.5	0.36	1.5	6.0
C11	1530	92.4	0.03	0.3	7.3
C112	1530	92.9	0.07	0.2	6.9
C5 - 1500/18min	1500	93.0	0.61	0.3	6.7
C8	1540	93.6	0.16	0.1	6.3
C83	1540	93.6	0.07	0.0	6.4
C7	1550	93.6	0.30	0.1	6.3
C82	1540	93.7	0.18	0.1	6.2
C102	1545	93.8	0.16	0.1	6.0
C10	1545	94.0	0.00	0.0	6.0
C72	1550	94.5	0.04	0.0	5.5
C73	1550	94.6	0.04	0.0	5.4
C9	1560	95.6	0.14	0.0	4.4

Vo is volume of open porosity, Vc is volume of closed porosity, s is standard deviation calculated from 3 measurements

Appendix 9: Measured relative density, open and closed porosity for 3Y 100 MPa CIP

Sample	Temperature [°C]	Relative density [%]	s [-]	V_O [%]	V_C [%]
Hx0	800	44.0	0.17	54.3	1.7
Hx1	1320	79.7	0.17	20.2	0.1
Hx3	1350	83.4	0.14	16.6	0.1
Hx4	1370	84.7	0.08	14.7	0.6
Hx5	1390	86.6	0.18	12.6	0.8
Hx8	1405	87.3	0.25	12.2	0.5
Hx6	1410	90.2	0.28	6.4	3.4
Hx103	1410	91.9	0.09	0.8	7.3
Hx102	1410	92.6	0.03	0.7	6.7
Hx10	1415	92.9	0.25	0.7	6.4
Hx9	1420	92.9	0.15	0.0	7.1
Hx93	1420	93.9	0.10	0.0	6.1
Hx92	1420	94.0	0.07	0.0	6.0
Hx7	1430	94.0	0.13	0.0	6.0

Vo is volume of open porosity, Vc is volume of closed porosity, s is standard deviation calculated from 3 measurements

Appendix 10: Measured relative density, open and closed porosity for 3Y 300 MPa CIP

Sample	Temperature [°C]	Relative density [%]	s [-]	V_O [%]	V_C [%]
H0	800	49.7	0.12	46.0	4.3
H1	1320	88.6	0.18	10.2	1.2
H4	1340	90.2	0.14	5.7	4.1
H42	1340	91.0	0.12	2.6	6.3
H43	1340	91.3	0.07	1.5	7.2
H34	1345	91.9	0.03	0.2	7.9
H33	1345	92.0	0.29	0.5	7.5
H22	1350	92.1	0.02	0.0	7.9
H3	1345	92.2	0.24	0.1	7.7
H32	1345	92.3	0.04	0.1	7.6
H2	1350	92.4	0.18	0.0	7.5
H23	1350	92.5	0.26	0.2	7.3
H52	1355	93.2	0.22	0.0	6.8
H5	1355	93.9	0.05	0.0	6.1

Vo is volume of open porosity, Vc is volume of closed porosity, s is standard deviation calculated from 3 measurements

Appendix 11: Measured relative density, open and closed porosity for 3YSB 100 MPa CIP

Sample	Temperature [°C]	Relative density [%]	s [-]	V_O [%]	V_C [%]
Ex0	800	48.3	0.9	50.8	0.9
Ex1	1455	83.1	0.2	16.4	0.4
Ex2	1465	85.0	0.2	14.4	0.5
Ex3	1475	88.3	0.1	11.3	0.4
Ex4	1490	90.4	0.2	7.9	1.7
Ex7	1500	91.2	0.1	6.6	2.2
Ex8	1505	92.5	0.1	0.7	6.8
Ex82	1505	92.8	0.0	1.1	6.1
Ex83	1505	92.9	0.1	0.8	6.3
Ex5	1510	92.9	0.2	0.2	6.9
Ex53	1510	93.0	0.0	0.4	6.5
Ex54	1510	93.1	0.0	1.1	5.8
Ex52	1510	93.1	0.2	0.7	6.3
Ex6	1520	94.1	0.1	0.0	5.9
Ex63	1520	94.3	0.1	0.1	5.6
Ex62	1520	94.6	0.0	0.0	5.3
Ex92	1530	95.6	0.1	0.1	4.3
Ex93	1530	95.5	0.1	0.1	4.4
Ex9	1530	95.0	0.3	0.0	5.0

Vo is volume of open porosity, Vc is volume of closed porosity, s is standard deviation calculated from 3 measurements

Appendix 12: Measured relative density, open and closed porosity for 3YSB 300 MPa CIP

Sample	Temperature [°C]	Relative density [%]	s [-]	V_O [%]	V_C [%]
E0	800	51.8	0.2	47.5	0.6
E1	1320	65.7	0.3	34.2	0.2
E2	1370	73.6	0.3	26.4	0.0
E5	1455	89.8	0.1	9.2	1.1
E7	1460	91.5	0.1	6.6	2.0
E6	1465	91.7	0.0	2.5	5.8
E62	1465	92.2	0.2	1.0	6.8
E8	1470	92.4	0.0	1.3	6.3
E64	1465	92.7	0.0	0.3	7.0
E63	1465	92.7	0.0	0.1	7.2
E82	1470	93.4	0.1	0.1	6.5
E83	1470	93.5	0.2	0.0	6.5
E4	1475	93.8	0.3	0.0	6.1
E42	1475	94.0	0.1	0.0	6.0
E3	1485	94.7	0.1	0.0	5.3
E9	1480	94.8	0.1	0.0	5.2
E32	1485	95.2	0.0	0.2	4.6

Vo is volume of open porosity, Vc is volume of closed porosity, s is standard deviation calculated from 3 measurements

Appendix 13: Measured relative density, open and closed porosity for 8Y 100 MPa CIP

Sample	Temperature [°C]	Relative density [%]	s [-]	V_O [%]	V_C [%]
Fx0	800	44.5	0.72	53.4	2.1
Fx1	1350	82.5	0.42	17.3	0.2
Fx3	1370	87.2	0.09	11.7	1.1
Fx9	1390	88.6	0.26	10.6	0.8
Fx2	1360	89.2	0.16	9.9	0.8
Fx6	1400	89.4	0.24	8.0	2.6
Fx8	1405	91.9	0.14	0.4	7.7
Fx63	1400	93.3	0.03	0.0	6.7
Fx62	1400	93.4	0.06	0.0	6.6
Fx82	1405	93.7	0.01	0.0	6.3
Fx5	1410	93.8	0.26	0.1	6.1
Fx83	1405	94.0	0.10	0.0	6.1
Fx52	1410	94.6	0.13	0.0	5.3
Fx54	1410	94.9	0.04	0.1	5.0
Fx53	1410	94.9	0.01	0.0	5.1
Fx10	1415	95.1	0.31	0.0	4.9
Fx9	1420	95.3	0.14	0.0	4.7
Fx102	1415	95.5	0.27	0.0	4.5
Fx103	1415	95.7	0.00	0.0	4.3

Vo is volume of open porosity, Vc is volume of closed porosity, s is standard deviation calculated from 3 measurements

Appendix 14: Measured relative density, open and closed porosity for 8Y 100 MPa CIP

Sample	Temperature [°C]	Relative density [%]	s [-]	V_O [%]	V_C [%]
F0	800	50.0	0.4	48.5	1.9
F1	1320	86.6	0.6	11.5	1.9
F6	1355	89.9	0.1	6.2	3.9
F4	1350	90.1	0.3	5.9	3.9
F3	1360	90.6	0.2	0.4	9.0
F42	1350	90.6	0.2	2.0	6.1
F43	1350	90.9	0.1	1.2	6.7
F63	1355	91.7	0.2	0.2	6.6
F62	1355	91.9	0.1	0.0	3.4
F2	1370	92.6	0.2	0.3	7.1
F5	1365	92.7	0.2	0.1	7.2
F52	1365	94.7	0.1	0.1	5.9
F32	1360	95.0	0.2	0.0	4.6
F33	1360	95.3	0.1	0.0	4.4
F22	1370	95.8	0.1	0.1	4.2
F8	1375	96.1	0.2	0.0	3.9
F7	1380	96.3	0.3	0.0	3.7

Vo is volume of open porosity, Vc is volume of closed porosity, s is standard deviation calculated from 3 measurements

Appendix 15: Measured relative density, open and closed porosity for 8YSB 100 MPa CIP

Sample	Temperature [°C]	Relative density [%]	s [-]	V_O [%]	V_C [%]
Gx0	800	48.0	0.61	51.3	0.7
Gx2	1420	87.2	0.28	11.7	1.1
Gx7	1435	90.1	0.03	8.1	1.8
Gx6	1445	90.1	0.14	6.8	3.1
Gx3	1440	90.5	0.13	6.4	3.1
Gx4	1450	91.5	0.27	3.4	5.1
Gx5	1455	92.2	0.12	1.3	6.5
Gx1	1460	92.8	0.12	0.5	6.7
Gx12	1460	93.4	0.21	0.1	6.5
Gx92	1465	93.7	0.20	0.0	6.3
Gx9	1465	93.7	0.08	0.1	6.2
Gx13	1460	93.7	0.02	0.2	6.1
Gx8	1470	93.8	0.26	0.0	6.2
Gx82	1470	94.2	0.04	-0.1	5.9
Gx83	1470	94.3	0.13	0.1	5.6
Gx10	1480	94.5	0.12	0.2	5.2
Gx102	1480	94.8	0.05	0.0	5.2

Vo is volume of open porosity, Vc is volume of closed porosity, s is standard deviation calculated from 3 measurements

Appendix 16: Measured relative density, open and closed porosity for 8YSB 300 MPa CIP

Sample	Temperature [°C]	Relative density [%]	s [-]	V_O [%]	V_C [%]
G0	800	52.7	0.3	46.9	0.4
G1	1400	90.2	0.1	7.5	2.4
G53	1405	89.9	0.1	6.7	3.4
G52	1405	90.2	0.3	5.8	4.0
G5	1405	90.8	0.2	6.6	2.7
G33	1410	90.9	0.1	1.3	7.8
G32	1410	90.8	0.2	2.1	7.1
G3	1410	91.7	0.3	0.7	7.6
G6	1415	92.7	0.2	0.1	7.2
G62	1415	93.1	0.2	0.0	6.9
G42	1420	93.7	0.3	0.1	6.2
G4	1420	93.8	0.2	0.0	6.2
G9	1425	94.0	0.1	0.0	5.9
G7	1430	94.8	0.1	0.1	5.1
G8	1440	95.6	0.3	0.0	4.4
G2	1450	96.1	0.1	0.0	3.9
G22	1450	96.5	0.1	0.1	3.4

Vo is volume of open porosity, Vc is volume of closed porosity, s is standard deviation calculated from 3 measurements

9 LIST OF ABBREVIATIONS AND SYMBOLS

List of Abbreviations

HIP	Hot Isostatic Press
VdW	Van der Waals
E-C	Evaporation-condensation
SD	Surface diffusion
VD	Volume diffusion
PF	Plastic flow
GB	Grain boundary diffusion
C&G	Carter & Gleaser
MP	Mobility of pore
MGB	Mobility of grain boundary
BUT	Brno University of Technology
YSZ	Yttrium stabilized zirconia
IR	Infra red
AKP	Al_2O_3 powder AKP30
REY	Al_2O_3 powder Reynolds
TAI	Al_2O_3 powder Taimicron
3Y	ZrO_2 doped 3mol% Y_2O_3 powder TZ3Y
3YSB	ZrO_2 doped 3mol% Y_2O_3 powder TZ3YSB
8Y	ZrO_2 doped 8mol% Y_2O_3 powder TZ8Y
8YSB	ZrO_2 doped 8mol% Y_2O_3 powder TZ8YSB
S30CR	$MgAl_2O_4$ powder Baikalox S30CR

List of Symbols

t.d.	Theoretical density [kg.m-3]	m_1	Mass of dry sample [kg]
F_{VdW}	Van der Waals Force [N]	m_2	Mass of sample under water [kg]
A	Hamaker constant [J]	m_3	Mass of dried sample [kg]
R	Particle radius [m]	ρ_{rel}	Relative density [-]
D	Distance between particle surface [m]	V_o	Volume of open porosity [%]
μm	Micro meter	V_C	Volume of closed porosity [%]
wt.%	Weight percent	T_{H_2O}	Temperature of water [°C]
°C	Degrees of Celsius	ρ_{H_2O}	Density of water [kg.m-3]
MPa	Mega pascal	s	Standard deviation [-]
GPa	Giga pascal		
γ^{SG}	Interfacial solid/gas energy [J·m^{-2}]		
γ^{SS}	Interfacial solid/solid energy [J·m^{-2}]		
S	Surface area [m^2]		
σ	Stress [MPa]		
r	Radii of arcs on a surface [m]		
γ	Surface energy [J·m^{-2}]		
ψ	Dihedral angle [°]		
V_{TKDH}	Volume of tetrakaidecahedron [m^3]		
l_e	Edge length [m]		
λ_{crit}	Critical wavelength [m]		
r_c	Critical pore radius [m]		
V_{Pcrit}	Critical volume of porosity [m^3]		
l_{Pcrit}	Critical pore length [m]		
V_{Gcrit}	Volume of grain with l_{Pcrit} [m^3]		
P_{crit}	Critical porosity [%]		
n	Number of grains surrounging pore		
R_0	Radius of a circle circumscribing pore channel [m]		
ρ'	Circular arc of pore [m]		
η'	Distance of origin of radius ρ' [m]		
ρ	Geometrical factor of ρ' [-]		
η	Geometrical factor of η' [-]		
U	Geometrical factor of C&G's model		
P	Geometrical factor of C&G's model		
nm	nanometer		